J. Fluid Mech. (1989), *vol.* 200, *pp.* 511–562
Printed in Great Britain

Coherent structure of the convective boundary layer derived from large-eddy simulations

By HELMUT SCHMIDT AND ULRICH SCHUMANN
DLR, Institute of Atmospheric Physics, D-8031 Oberpfaffenhofen,
Federal Republic of Germany

(Received 3 March 1988)

Turbulence in the convective boundary layer (CBL) uniformly heated from below and topped by a layer of uniformly stratified fluid is investigated for zero mean horizontal flow using large-eddy simulations (LES). The Rayleigh number is effectively infinite, the Froude number of the stable layer is 0.09 and the surface roughness height relative to the height of the convective layer is varied between 10^{-6} and 10^{-2}. The LES uses a finite-difference method to integrate the three-dimensional grid-volume-averaged Navier–Stokes equations for a Boussinesq fluid. Subgrid-scale (SGS) fluxes are determined from algebraically approximated second-order closure (SOC) transport equations for which all essential coefficients are determined from the inertial-range theory. The surface boundary condition uses the Monin–Obukhov relationships. A radiation boundary condition at the top of the computational domain prevents spurious reflections of gravity waves. The simulation uses $160 \times 160 \times 48$ grid cells. In the asymptotic state, the results in terms of vertical mean profiles of turbulence statistics generally agree very well with results available from laboratory and atmospheric field experiments. We found less agreement with respect to horizontal velocity fluctuations, pressure fluctuations and dissipation rates, which previous investigations tend to overestimate. Horizontal spectra exhibit an inertial subrange. The entrainment heat flux at the top of the CBL is carried by cold updraughts and warm downdraughts in the form of wisps at scales comparable with the height of the boundary layer. Plots of instantaneous flow fields show a spoke pattern in the lower quarter of the CBL which feeds large-scale updraughts penetrating into the stable layer aloft. The spoke pattern has also been found in a few previous investigations. Small-scale plumes near the surface and remote from strong updraughts do not merge together but decay while rising through large-scale downdraughts. The structure of updraughts and downdraughts is identified by three-dimensional correlation functions and conditionally averaged fields. The mean circulation extends vertically over the whole boundary layer. We find that updraughts are composed of quasi-steady large-scale plumes together with transient rising thermals which grow in size by lateral entrainment. The skewness of the vertical velocity fluctuations is generally positive but becomes negative in the lowest mesh cells when the dissipation rate exceeds the production rate due to buoyancy near the surface, as is the case for very rough surfaces. The LES results are used to determine the root-mean-square value of the surface friction velocity and the mean temperature difference between the surface and the mixed layer as a function of the roughness height. The results corroborate a simple model of the heat transfer in the surface layer.

1. Introduction

The convective boundary layer (CBL) in the atmosphere arises if turbulence generated by buoyancy due to upward heat flux from the surface dominates relative to turbulence generated by mean shear. The convective motion in the CBL exhibits a coherent structure of convective circulations composed of 'updraughts' and 'downdraughts'. Buoyant updraughts with warm air rising in rather narrow columns are surrounded by larger areas which are slowly sinking as downdraughts. The updraughts are called 'plumes' if they extend from the warm surface far up into the boundary layer or 'thermals' if they are finite elements of buoyant fluid rising in the CBL (Turner 1986). These structures are important to transfer processes in the atmosphere (Wyngaard 1985; Chatfield & Brost 1987; Nieuwstadt & de Valk 1987). In this paper, we investigate the spatial structure and aspects of its time derivatives in the dry CBL for zero mean wind over a homogeneous surface and study the influence of surface roughnesses. For this purpose, we use large-eddy simulations (LES) based on the method described in Schumann *et al.* (1987).

In the atmosphere, the CBL is capped by an inversion layer with stably stratified air above. As shown by Deardorff (1970) and others, the relevant scales for a CBL are the height z_i of the inversion above the surface (or the height at which the vertical heat flux reaches its minimum value) and the convective velocity and temperature scales:

$$w_* = (\beta g z_i Q_s)^{\frac{1}{3}}, \quad T_* = \frac{Q_s}{w_*}, \tag{1}$$

where g is the gravitational acceleration, β is the volumetric expansion coefficient ($\beta \approx 1/T$ as a function of temperature T in air) and Q_s denotes the surface 'temperature flux', $Q_s = \langle w'T' \rangle_s$. The angle brackets denote ensemble mean values. These scales apply in particular for the 'mixed layer' which extends approximately from $0.1z_i$ to $0.9z_i$. The effect of the surface roughness height z_0 may be noticeable in the 'surface layer' between the mixed layer and the rough surface. In the 'interfacial layer' which encloses the inversion above the mixed layer, static stability represents an important additional parameter.

Much is known about the CBL from observations in the atmosphere. The results of several field experiments are summarized in Caughey (1982). Our knowledge has also been increased by the laboratory experiments of Willis & Deardorff (1974, 1979), Deardorff & Willis (1985) and Adrian, Ferreira & Boberg (1986); the LES of Deardorff (1972, 1973, 1974), Schemm & Lipps (1976), Moeng (1984), Moeng & Wyngaard (1986), Nieuwstadt & de Valk (1987), Schumann *et al.* (1987), and Mason (1987); and by the second- and third-order closure models of Mellor & Yamada (1974), Zeman & Lumley (1976), André *et al.* (1978), Chen & Cotton (1983), and Finger & Schmidt (1986). As a result, we have a fairly complete knowledge of the vertical profiles of second- and third-order moments of turbulent fluctuations, horizontal spectra and of probability distributions of vertical velocity and temperature fluctuations at a given height. Some discussion continues on the magnitude of horizontal velocity fluctations (Deardorff & Willis 1985) and the profile of velocity skewness $\langle w^3 \rangle / \langle w^2 \rangle^{\frac{3}{2}}$ (Hunt, Kaimal & Gaynor 1988) and we shall add new information to these discussions.

The spatial structure of the updraughts and downdraughts has been observed in the atmosphere as summarized by Kaimal *et al.* (1976), Lenschow & Stephens (1980), Wilczak & Tillman (1980), Greenhut & Khalsa (1982, 1987), Grossman (1982, 1984), Crum, Stull & Eloranta (1987) and others. Also the LES results, in particular those

of Deardorff (1972) have given insight into the spatial and temporal structure. Some controversy can be traced in the older literature on whether updraughts are plumes with a continuous vertical structure or thermals rising intermittently like bubbles in the CBL (Ludlam & Scorer 1953). According to the more recent studies, updraughts are mainly composed of plumes which often extend through the depth of the well-mixed layer up to the capping inversion. Thermals rising from the surface either merge together into plumes or are destroyed in the lower part of the boundary layer (Lenschow & Stephens 1980; Wilczak & Tillman 1980). The plumes have highly convoluted turbulent boundaries with strong lateral entrainment (Crum *et al.* 1987). The rising air spreads out laterally as it reaches the inversion base, produces a dome-like depression at the interface, and returns as a downdraught along the sides of the plumes. The domes at tops of penetrating plumes have been clearly observable by radar (Konrad 1970) and typically have separation distances of order z_i. Downdraughts transport fluid components from above the inversion down to heights of order $0.25z_i$ and less (Grossman 1984). Details of the entrainment process and the relative importance of turbulence and waves are discussed in Carruthers & Moeng (1987) and earlier papers cited therein.

Flow visualisations of laboratory convection (Willis & Deardorff 1979), and the LES of Deardorff (1972) and in particular Mason (1987) confirm these findings for the upper part of the CBL but indicate that a coherent polygonal 'spoke' pattern arises in the lower half of the CBL as has been observed in less turbulent states for moderate Rayleigh numbers (2×10^5) in high-Prandtl-number Rayleigh–Bénard convection by Busse & Whitehead (1974). Plumes or thermals rise from cross-points or 'hubs' (Willis & Deardorff 1979) of the spokes. The spokes form polygonal open cells similar in structure to but at much smaller scale than the open mesoscale cellular cloud pattern (Krishnamurti 1975; Busse 1978). There is only a little evidence available that shows polygonal spoke patterns in the atmosphere (Woodcock & Wyman 1947; Lyons & Pease 1972; Webb 1977; Wilczak & Tillman 1980; Grossman 1982) (see also the discussion in Willis & Deardorff 1979). As the laboratory investigations of Willis & Deardorff (1979) are valid for a Rayleigh number below 10^9 while the Rayleigh number in a typical atmospheric CBL is greater than 10^{16} it is not clear whether these spoke patterns are realistic features of the atmosphere.

It remains to be shown whether the simulations of Mason (1987) apply to an atmospheric CBL because he uses rather large subgrid-scale (SGS) diffusivities (in comparison to Lilly's 1967 theory) which might effectively represent a limited Rayleigh number. He observes an intensification of the spoke pattern for increasing diffusivity. Mason & Callen (1986) and Mason (1987) suggest that large SGS diffusivities are necessary to avoid excessive finite-difference errors in such LES. However, Mason & Thomson (1987), in a LES of the neutral planetary boundary layer, find the results for small SGS diffusivities most satisfactory.

The quantitative structure of updraughts and downdraughts of the CBL has been investigated by conditional sampling (Coulman 1970; Lenschow & Stephens 1980; Greenhut & Khalsa 1982, 1987; Mahrt & Paumier 1984; Grossman 1984; Wilczak & Businger 1983, 1984; Young 1988 and Hunt *et al.* 1988). For example, Greenhut & Khalsa (1987) analysed flight data and identified updraughts (downdraughts) at flight path fractions where the vertical velocity exceeds a certain threshold value in magnitude along a certain minimum length of the flight path. They report statistics on the horizontal diameters of updraughts and downdraughts, horizontal distances between these structures, averages of vertical velocity and temperature within these events and the individual contributions to vertical fluxes by these structures.

However, the vertical structure of convection cannot be determined from flight data obtained with a single airplane; this would require simultaneous measurements at several heights. Nor do the previous analyses provide information on the temporal structure and on horizontal motions and horizontal fluxes associated with updraughts. Such information will be determined in this paper. Previous conditional-sampling results depend strongly on the sampling criteria. We shall introduce a multidimensional conditional-sampling technique which is only weakly dependent on the parameters of the sampling criterion.

The influence of sampling criteria is totally avoided in spatial correlation functions but such functions do not distinguish between updraughts and downdraughts. The available correlation measurements are restricted to one-dimensional correlation functions with respect to either horizontal (Deardorff & Willis 1985) or vertical separation (Hunt 1984). In this paper, we will determine three-dimensional correlation functions.

Little is known about the influence of surface roughness on the CBL in the absence of mean wind. It is generally assumed (Wyngaard 1985) that the effect of the surface roughness is small with respect to the mixed layer inside the CBL. However, surface roughness does influence the turbulent exchange processes at the surface itself. In a recent paper, Schumann (1988) has set up a model for the surface layer of the CBL. This model is based on the concept of conditional averaging. It requires data on horizontal motions in the surface layer induced by updraughts and on the related momentum and vertical heat flux and spatial structure of the pressure in the surface layer. The present analysis arose from a need to provide quantitative data on these properties. Schumann had to estimate these data by calibrating the results from observed mean values of the turbulent fluctuations. From the model he determined the mean friction velocity at the surface related to the thermal motion and the mean temperature difference between the mixed layer and the surface. In this paper we shall verify these results.

In the next section we shall describe the LES method and the initial and boundary conditions used for the present study. This simulation is performed with a computational grid which fully exploits the capacity of a CRAY-XMP computer. Section 3 describes the results. The computed mean profiles of turbulent fluctuations and horizontal spectra will be compared to results obtained in experiments and earlier simulations. We then determine the three-dimensional structure of the CBL in terms of instantaneous flow fields, three-dimensional correlation functions, and conditionally averaged fields related to updraughts and downdraughts. Finally we shall determine the influence of surface roughnesses by means of a parameter study. Section 4 summarizes the conclusions and relates them to earlier studies.

2. The large-eddy simulation method

The method (the MESOSCOP program) used in this paper has been developed by Schmidt (1988) and Schumann *et al.* (1987). Except for the SGS model, it is described in Schumann *et al.* (1987) together with verifying results in comparison to the laboratory experiments of Deardorff & Willis (1985) and several other test cases. Here, we repeat the essential features of the method and describe the SGS-model.

2.1. *The basic equations*

The basic equations describe the mass and momentum balances and the first law of thermodynamics in terms of grid-averaged velocities $u_i = (u, v, w)$ and temperature

T as a function of the coordinates $x_i = (x, y, z)$ and of time t. The Oberbeck–Boussinesq approximation is used, i.e. density ρ is assumed to be constant except for buoyancy. In this approximation, temperature T corresponds to the potential temperature in the atmospheric boundary layer (Busse 1978). The balance equations are

$$\frac{\partial \overline{u}_j}{\partial x_j} = 0, \tag{2}$$

$$\frac{\partial \overline{u}_i}{\partial t} + \frac{\partial (\overline{u}_j \overline{u}_i)}{\partial x_j} = -\frac{1}{\rho}\frac{\partial \overline{p}}{\partial x_i} + \frac{\partial}{\partial x_j}\left(\nu \frac{\partial \overline{u}_i}{\partial x_j} - \overline{u_i'' u_j''}\right) + \beta g \overline{T} \delta_{i3}, \quad i = 1, 2, 3, \tag{3}$$

$$\frac{\mathrm{D}\overline{T}}{\mathrm{D}t} \equiv \frac{\partial \overline{T}}{\partial t} + \frac{\partial (\overline{u}_j \overline{T})}{\partial x_j} = \frac{\partial}{\partial x_j}\left(\mu \frac{\partial \overline{T}}{\partial x_j} - \overline{u_j'' T''}\right). \tag{4}$$

Here, p is the pressure, g is the gravitational acceleration, $\beta = -(\partial \rho / \partial T)/\rho$ is the volumetric expansion coefficient, ν and μ are the constant molecular diffusivities of momentum and heat (included here for completeness only). The coordinate $x_3 = z$ points vertically upwards. The bar denotes the average over a computational grid cell and the double primes the deviations thereof.

Properly, one should be more precise in defining the grid average and distinguish between volume and surface mean values as in Schumann (1975). However, in the present study we shall use equal grid spacings in all three directions and fine resolution so that such details do not matter. Coriolis forces are neglected because they have very small effects at zero mean wind in the CBL (Moeng & Wyngaard 1986).

2.2. *The subgrid-scale model*

The subgrid-scale (SGS) fluxes are approximated in terms of the resolved fields and the SGS kinetic energy $\overline{E''} \equiv \overline{u_i''^2}/2$, for which we integrate the closed model equation

$$\frac{\mathrm{D}\overline{E''}}{\mathrm{D}t} = -\overline{u_i'' u_j''}\frac{\partial \overline{u}_i}{\partial x_j} + \beta g \overline{w'' T''} + \frac{\partial}{\partial x_i}\left[\frac{5}{3} l c_{3m} \overline{E''}^{\frac{1}{2}} \frac{\partial \overline{E''}}{\partial x_i}\right] - c_{\epsilon m} \frac{\overline{E''}^{\frac{3}{2}}}{l}. \tag{5}$$

The turbulent heat and momentum fluxes and their respective anisotropic components

$$\overline{A_{ij}''} = \overline{u_i'' u_j''} - \tfrac{2}{3}\delta_{ij}\overline{E''}, \quad i = 1, 2, 3, \quad j = 1, 2, 3, \tag{6}$$

are determined from the following set of algebraically approximated second-order closure (SOC) equations:

$$0 = -(1 - c_{Gm})\tfrac{2}{3}\overline{E''}\left(\frac{\partial \overline{u}_i}{\partial x_j} + \frac{\partial \overline{u}_j}{\partial x_i}\right) + (1 - c_{Bm})[\beta g(\delta_{i3}\overline{u_j'' T''} + \delta_{j3}\overline{u_i'' T''} - \tfrac{2}{3}\delta_{ij}\overline{u_3'' T''})] - c_{Rm}\frac{\overline{E''}^{\frac{1}{2}}}{l}\overline{A_{ij}''}, \tag{7}$$

$$0 = -(1 - c_{GT})\tfrac{2}{3}\overline{E''}\frac{\partial \overline{T}}{\partial x_i} + (1 - c_{BT})\beta g \overline{T''^2}\delta_{i3} - c_{RT}\frac{\overline{E''}^{\frac{1}{2}}}{l}\overline{u_i'' T''}, \tag{8}$$

$$0 = -2\overline{u_j'' T''}\frac{\partial \overline{T}}{\partial x_j} - c_{\epsilon T}\frac{\overline{E''}^{\frac{1}{2}}\overline{T''^2}}{l}. \tag{9}$$

This set of SOC equations results from the more complete system deduced by Gibson & Launder (1976) by using arguments as given in Mellor & Yamada (1974),

	Model proposed by						
	D	SL	S	DM	Ma	GS	SS
c_v	0.0646	0.0645	0.0667	0.10	—	0.042	0.0856
$c_{\epsilon m}$	0.7	0.7	0.7	0.7	—	0.634	0.845
c_S	0.14	0.14	0.143	0.194	0.16/0.46	0.104	0.165
c_γ	0.161	0.161	0.167	—	—	0.107	0.204
$c_{\epsilon T}$	0.42	0.58	1.2	—	—	—	2.02
c_{ST}	0.221	0.221	0.227	0.336	$1c_s/2c_s$	0.166	0.255

TABLE 1. Coefficients of SGS models. The abbreviations denote the various models proposed by Deardorff (1974): D; Schemm & Lipps (1976): SL; Sommeria (1976): S; Deardorff (1980) and Moeng (1984): DM; Mason (1987): Ma; Grötzbach & Schumann (1979): GS; and this paper: SS. Mason (1987) varied the coefficient values in a range as indicated. Further coefficient values used in the present paper: $c_{Gm} = 0.55$, $c_{Bm} = 0.55$, $c_{GT} = 0.50$, $c_{BT} = 0.50$, $c_{Rm} = 3.50$, $c_{RT} = 1.63$, $c_{3m} = 0.2$, $c_l = c_{\epsilon m}$.

Sommeria (1976) and Schemm & Lipps (1976). In particular it is assumed that local time derivatives, advective fluxes and anisotropic production rates contribute little to the anisotropic components of the fluxes. These approximations can be justified by scale analysis (Schemm & Lipps 1976). The weakest point is probably the neglect of anisotropic production rates which will become important near the surface. However, for the CBL without mean shear, the present set of equations gives reasonable results even if applied not only to SGS contributions but to the total turbulent fluxes (Finger & Schmidt 1986). Since time derivatives and advective fluxes are neglected, these equations define a system of linear equations for the turbulent fluxes. The neglect of anisotropic shear contributions to the production rates decouples the horizontal fluxes from the vertical ones and the system can be solved explicitly in an effective manner, therefore. The explicit equations are given in Appendix A.

The lengthscale l is prescribed as a function of height z above the surface and of the average mesh spacing Δ by

$$l = \min(\Delta, c_l z), \quad \Delta = \tfrac{1}{3}(\Delta x + \Delta y + \Delta z). \tag{10}$$

Except for c_{3m} and c_l, all essential model coefficients can be determined from the spectra of kinetic energy and temperature variance in the inertial–convective subrange of locally isotropic turbulence. In Appendix B we show this in detail and compare the results with previous proposals. The value of c_{3m} is taken from Deardorff (1974). For the reasons given in Appendix C, we use $c_l = c_{\epsilon m}$ unless stated otherwise. The standard values of the model coefficients are summarized in table 1. Deardorff (1980) and others have limited the lengthscale for strong static stability. We have tested such proposals but found them of little advantage in the context of SOC models in which stability effects enter directly into the SGS fluxes (Schmidt 1988).

2.3. *The numerical solution method and boundary conditions*

The numerical integration scheme is described in Schumann *et al.* (1987). It is based on an equidistant staggered grid and finite-difference approximations. The momentum and continuity equations are approximated by second-order central differences in space which conserve mass, momentum and energy very accurately. Time integration is performed using the Adams–Bashforth scheme. The balance equations for temperature and for SGS kinetic energy are approximated by the second-order upwind-scheme of Smolarkiewicz (1984). A first-order upwind-scheme

would cause unacceptable numerical diffusion while the present scheme eliminates first-order numerical diffusion.

The computational domain extends horizontally and vertically over a finite domain of size $X \times X \times Z$. At the lateral boundaries, periodicity is assumed. At the top, free-slip boundary conditions are used for the horizontal velocity components; the vertical derivative of temperature is prescribed according to the mean temperature profile; the vertical diffusive flux of SGS kinetic energy is set to zero; pressure and vertical velocity are connected by means of the radiation boundary condition of Bougeault (1983) and Klemp & Durran (1983) which reduces the reflection of gravity waves. At the bottom, the heat flux Q_s determines the SGS flux at this surface, and the vertical fluxes of horizontal momentum are evaluated from the Monin-Obukhov relationships as described in Appendix D. The present study assumes equal values for the roughness heights which are effective for momentum and heat transfer. In the interior of the domain, pressure is computed by solving a discrete Poisson equation employing fast Fourier-transform algorithms.

2.4. *Initial conditions and computational aspects*

The initial temperature profile represents a constant-temperature mixed layer topped by a layer of uniform stability where $\mathrm{d}\langle T\rangle/\mathrm{d}z > 0$ is a constant. We intend to present all results non-dimensionally in terms of the convective scales, see (1). We expect to achieve an asymptotic state after a time of order $6z_i/w_*$ when the normalized turbulence profiles become stationary. However, the time-dependence of z_i makes it unsuitable for normalizing the initial conditions and time axis. Therefore, we design the initial conditions such that we obtain a boundary-layer height of approximately $z_{i0} = 1600$ m at the time of evaluation and use this height for normalization, while the final value of z_i is unknown. From preliminary runs we found that an initial mixed-layer height of 1350 m results in $z_i \approx z_{i0}$ at the final time. The convective scales related to Q_s and z_{i0} and the non-dimensional time t_* are defined by

$$w_{*0} = (\beta g Q_s z_{i0})^{\frac{1}{3}}, \quad T_{*0} = \frac{Q_s}{w_{*0}}, \quad t_* = t w_{*0}/z_{i0}. \tag{11}$$

The Brunt-Väisälä frequency $N = (\beta g \mathrm{d}\langle T\rangle/\mathrm{d}z)^{\frac{1}{2}}$ in the stable layer can be used to define a 'convective Froude number'

$$Fr = w_{*0}/(N z_{i0}). \tag{12}$$

The values selected are typical for a sunny day in southern Germany: $Q_s = 0.06$ K ms^{-1}, $z_{i0} = 1600$ m, $\mathrm{d}\langle T\rangle/\mathrm{d}z = 0.003$ K m^{-1}, $T_0 = 650 T_{*0} \approx 26.6$ °C, $\beta = 1/300$ K^{-1}, $g = 9.81$ m s^{-2}, $\nu = 15 \times 10^{-6}$ m^2 s^{-1}, $\mu = 21.4 \times 10^{-6}$ m^2 s^{-1}, $z_0 = 10^{-4} z_{i0}$. These values imply $w_{*0} = 1.46$ m s^{-1}, $T_{*0} = 0.041$ K, $N = 0.0099$ s^{-1}, $Fr = 0.0922$. Since the Reynolds number $w_{*0} z_{i0}/\nu = 1.6 \times 10^{11}$ and the Rayleigh number $Ra = (\beta g T_* z_i^3)/(\nu\mu) = 1.7 \times 10^{16}$ are very high, molecular diffusivities are unimportant and, hence, the results depend solely on z_i/z_0 and Fr as independent characteristic numbers.

The computational domain extends horizontally over a domain of size $X = 8000$ m $= 5 z_{i0}$ in the x- and y-directions, and vertically from height $z = 0$ to $z = Z = 2400$ m $= 1.5 z_{i0}$. Thus the domain accommodates several plumes at a given time. The vertical extent is small but this is permissible because of the radiation boundary condition at the top.

The initial temperature and velocity fields contain disturbances in terms of random numbers r equally distributed between -0.5 and 0.5 to initiate the

convective motion and the initial value for the SGS energy is set to an arbitrary but positive function:

$$\left.\begin{aligned} &T = T_0 + 0.1\, r(1-z/z_{i1})\, T_{*0}; \quad w = 0.1\, r(1-z/z_{i1})\, w_{*0} \quad \text{for} \quad 0 < z \leqslant z_{i1} \\ &T = T_0 + (z-z_{i1})\frac{\mathrm{d}\langle T\rangle}{\mathrm{d}z}; \quad w = 0 \quad \text{for} \quad z > z_{i1}, \\ &\overline{E''} = 0.1\, w_{*0}^2(1-z/Z), \end{aligned}\right\} \tag{13}$$

where $z_{i1} = 0.844 z_{i0}$. The initial velocity field is then adjusted to the continuity equation using the gradient of a pressure which satisfies the corresponding Poisson equation (Schumann *et al.* 1987).

The number of grid cells is $160 \times 160 \times 48$ cells, where the last number counts the grid cells in the vertical direction. Thus the grid width is $\Delta = z_{i0}/32 = 50$ m in all three directions. The time step Δt is set to $0.0025 z_{i0}/w_{*0}$, which is a little less than the maximum time step allowed for numerical stability according to linear stability analysis.

The code is run on a CRAY-XMP using 8 MW (Million words) of main storage. The total integration up to $t_* = 7$ requires 65000 s of computation time and includes 2800 time steps. The total amount of data required per time step amounts to 34 MW and thus exceeds the available main storage. Therefore, the data are split into two-dimensional (x, z) slabs which are swapped between main storage and secondary storage. The programming of the input/output operations turns out to be the crucial aspect of such simulations. Without special treatment, the input/output waiting time exceeds the computation time by an order of magnitude and this would make such simulations economically unfeasible. We use either direct access to a fast secondary storage device or asynchronous buffered sequential input/output to transfer the integration fields between disks and main storage. The actual selection depends on priority considerations of the job stream on our computer. In both cases, the input/output waiting time amounts to less than 7% of the computation time, which is quite acceptable.

3. Results

3.1. *Mean profiles*

We first compare results in terms of vertical profiles with previous investigations to show that the simulations give realistic results for a CBL. Mean values over all points in one horizontal plane approximate ensemble mean values and are denoted by brackets, e.g. $\langle f\rangle = \langle f\rangle(z)$ denotes a vertical mean profile of any quantity f. Primes denotes either local deviations from these mean values or root-mean-square (r.m.s.) values. For example, $T'(z)$ represents $\langle (T-\langle T\rangle)^2\rangle^{\frac{1}{2}}$. The inversion height z_i is determined in the model as that height where the vertical heat flux assumes its (negative) minimum. This height increases approximately linearly with time from $z_i = 0.875 z_{i0}$ initially to $z_i = 1.03 z_{i0}$ at time $t_* = 7$.

Figure 1 shows the mean temperature profile at the initial time and at $t_* = 6$. The increase in normalized temperature during the course of integration amounts to approximately 7.0 in the mixed layer. It is thus only a few percent larger than the value t_* which one expects if the constant heat input is equally distributed over the height z_{i0}. The larger temperature increase is due to heat stored initially above the mixed layer and entrained from there downwards. As a consequence of this entrainment, a sharp local inversion has been formed with enhanced stability. The

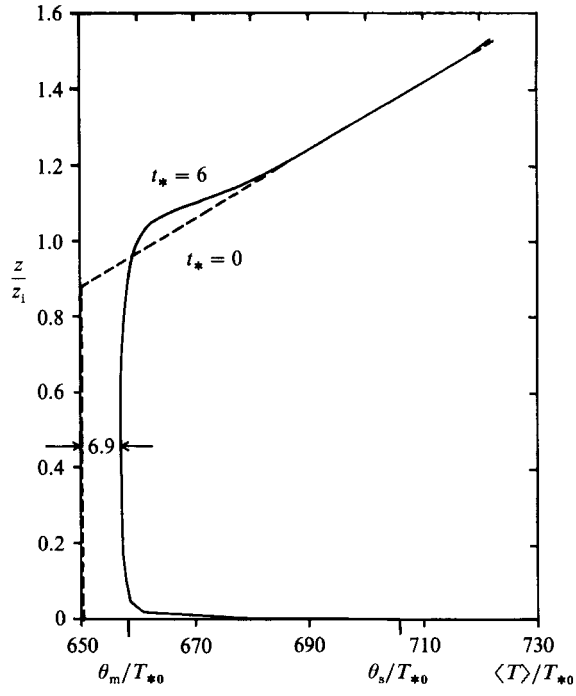

FIGURE 1. Mean temperature $\langle T(z)\rangle$ versus height at initial time (- - - - -) and at time $t_* = tw_{*0}/z_{i0} = 6$ (——). For both profiles, the vertical coordinate is normalized with the inversion height z_i at time $t_* = 6$. The mean temperature θ_m of the mixed layer and the mean surface temperature θ_s are indicated for $t_* = 6$.

surface temperature θ_s, which results from equation (D2), is much bigger than the mixed layer temperature θ_m. We shall come back to this issue in §3.6.

The vertical turbulent heat flux is plotted versus height in figure 2 in comparison to laboratory and atmospheric data. The bars indicate that the scatter of the numerical results between non-dimensional times 6 and 7 is reasonably small. The general trend is as to be expected. The vertical profile is close to linear up to $z/z_i < 0.95$. The linear profile implies a constant heating rate in the mixed layer and is thus an indicator for the stationarity of the turbulent state in the mixed layer. Near the inversion, the maximum negative entrainment heat flux amounts to $-(0.17 \pm 0.02) w_* T_*$. Field experiments show corresponding values varying between zero and -0.4, see Caughey & Palmer (1979) and Wilczak & Businger (1983). Our results are in close agreement with the LES result, -0.13, of Deardorff (1974) and -0.17 of Moeng (1984). Above the inversion, the heat flux is very small but positive; we shall discuss this aspect later. The dashed curve represents the SGS contribution. At the surface, the resolved vertical velocity vanishes and therefore all the flux is transported by SGS contributions at this level. Above this level, the mean SGS flux is very small. The SGS flux is negative near the inversion. We shall see that this is not consistent with the resolved heat flux at small scales, but the SGS flux is small so that this aspect is not important. For comparison we have included results from laboratory measurements (Deardorff & Willis 1985) and data from aircraft measurements (Lenschow, Wyngaard & Pennell 1980) for two strongly convective cases in which the value of the boundary-layer height is more than 250 times larger

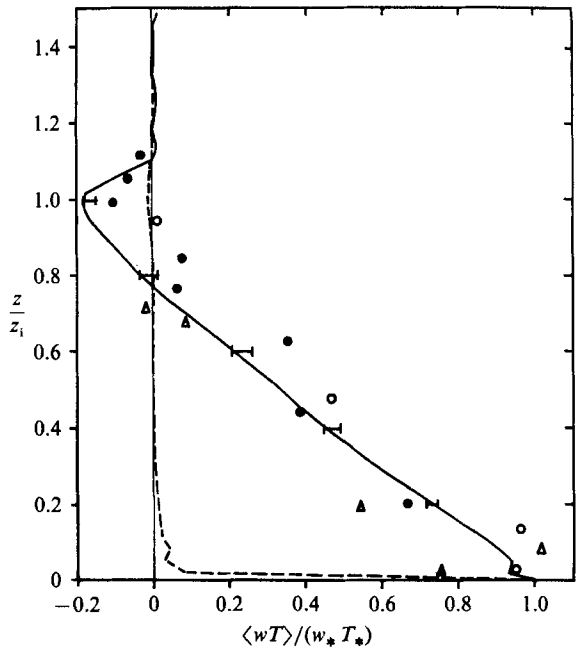

FIGURE 2. Normalized vertical heat flux versus height: ——, LES-result; - - - - -, SGS-part; both for $t_* = 6.5$. The error bars indicate the scatter of the mean profiles in the time period $t_* = 6$–7. Solid symbols denote laboratory measurements by Deardorff & Willis (1985), open symbols represent aircraft measurements by Lenschow *et al.* (1980) (○, 24 February 1975; △, 16 February 1975).

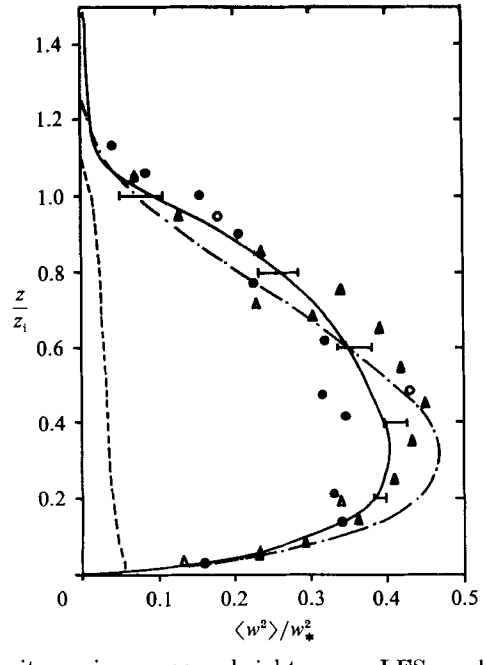

FIGURE 3. Vertical velocity variance versus height: ——, LES result for $t_* = 6.5$, the error bars indicate the scatter of the mean profiles in the time period $t_* = 6$–7; - - - - -, SGS part; solid symbols denote laboratory measurements of Willis & Deardorff (1974), case S1 (▲) and of Deardorff & Willis (1985) (●). The open symbols represent aircraft measurements of Lenschow *et al.* (1980) (○, 24 February 1975; △, 16 February 1975); –·–·–, interpolation curve $\langle w^2\rangle/w_*^2 = 1.8(z/z_i)^{\frac{2}{3}}(1 - 0.8z/z_i)^2$ proposed by Lenschow *et al.* (1980).

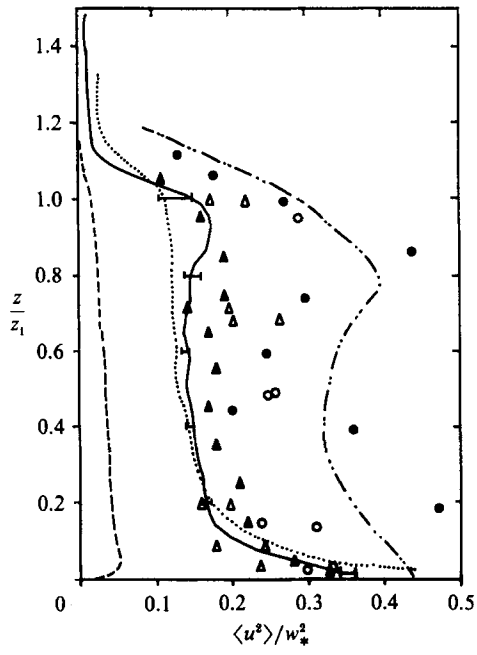

FIGURE 4. Horizontal velocity variance versus height. Curves and symbols as in figure 3 except for –·–·–, which represents the mean value of field measurements as reported by Caughey & Palmer (1979). ····· depicts the LES results for case 1 in Deardorff (1980). The open symbols represent aircraft measurements of both horizontal velocity components.

than the Obukhov length. The LES results are well within the wide range of the experimental data.

Figure 3 shows the profile of vertical velocity variance together with the SGS contribution and experimental data. The LES result seems to agree with the experimental data even better than the interpolation curve deduced from various measurements in the atmosphere by Lenschow *et al.* (1980). The SGS contribution is largest near the surface but amounts to less than 15% of the maximum total variance which is a small fraction. In Appendix C, we have shown that the SGS variance should stay below 1.8 $(z/z_i)^{\frac{2}{3}}$ if forced only by buoyancy. The fact that the SGS variance reaches this curve near the surface indicates that fluctuating shear produces an essential fraction of this variance. Above $z/z_i = 0.4$, the variance decreases slowly and is very small above the inversion. Hence, the top boundary condition in the numerical scheme successfully radiates gravity waves out of the computational domain.

The variance of the horizontal velocity fluctuations, see figure 4, is generally smaller than those of the vertical component because buoyancy forces excite directly only the vertical component while the horizontal component gains energy solely by the effect of pressure fluctuations. Only near the surface does a layer form in which the horizontal velocity fluctuations are larger than the vertical ones. The deviation between the simulation and experimental data are larger in this case. The large values obtained by Deardorff & Willis (1985) cannot be created by buoyancy forces alone. We have reasons to assume that the large horizontal velocity fluctuations in the tank experiment are caused by shear due to large-scale motions induced by horizontal variations of the surface heat flux. J. W. Deardorff (1987, personal

communication) informed us that the surface temperature at the bottom of the water tank exhibits variations of the order 0.3 K $\approx 2T_*$. Schmidt (1988) found that such variations may explain the larger horizontal velocity fluctuations. The older measurements of Willis & Deardorff (1974) are much closer to the numerical results. We have included the data points from their experiment S1 because in that experiment the Froude number was about 0.091 and thus close to the value 0.0922 in our LES, whereas the Froude number is approximately 0.0625 in experiment S2 of Willis & Deardorff (1974). The various data indicate a slight increase of both the horizontal and vertical velocity variance with decreasing Froude number. The experiments of Adrian *et al.* (1986) for non-penetrative convection between two horizontal walls can be considered as applying for zero Froude number and they exhibit, in fact, the largest velocity fluctuations both horizontally and vertically. The relatively small horizontal velocity fluctuations found by Willis & Deardorff (1974) were the reason why Deardorff & Willis (1985) repeated their laboratory investigations. They conjectured that the sidewalls of the water tank limited the horizontal velocity fluctuations in their previous experiment. In our case, the horizontal extent of the computational domain is rather larger ($X/z_{i0} = 5$) and periodic boundary conditions do not limit horizontal velocity fluctuations, but we get still the same results as Willis & Deardorff (1974). Therefore, we do not believe that the sidewalls of the water tank adversely affect Willis & Deardorff's data. The data summarized by Caughey & Palmer (1979) are obtained from various field experiments. Most atmospheric data are obtained for some finite mean wind speed with shear at the surface which is an additional source of turbulence. However, our results are in very good agreement with the data obtained by Lenschow *et al.* (1980) from aircraft measurements over a sea surface. Also Deardorff's (1980) LES of the dry CBL confirms our results but shows considerably enhanced turbulence variance near the inversion for a stratocumulus-capped mixed layer. We therefore conclude that the present method correctly simulates the horizontal velocity variance for a dry CBL with zero mean wind speed and strictly homogeneous surfaces.

The variance of the temperature fluctuations is shown in figure 5. Temperature fluctuations are produced by the negative product of heat flux and temperature gradient. This product is large near the surface and at the inversion. It is small in the middle of the CBL and even negative in the upper part of the mixed layer where heat is transported counter to the negative gradient of the mean temperature (Schumann 1987). This explains the general shape of the profile. Near the surface, the simulated results are only little smaller than the experimental findings from field observations (Kaimal *et al.* 1976). Here, the SGS contribution is essential. In the mixed layer, the simulated results are small in comparison to the measurements of Deardorff & Willis (1985) but again agree well with those of Willis & Deardorff (1974). Our mixed-layer results are consistently smaller by at least a factor of two than those from measurements in the atmosphere (Guillement *et al.* 1978; Caughey & Palmer 1979; Lenschow *et al.* 1980; Druilhet *et al.* 1983). It should be noted, however, that T_* is typically less than 0.1 K in the atmosphere so that it is unlikely that experiments will provide sufficient accuracy at a level of $T' \approx T_*$. The SGS contribution is negligible above $z/z_i > 0.05$. At the inversion we again find good agreement with the results of Willis & Deardorff (1974) while the results of Deardorff & Willis (1985) are significantly smaller. The generation of temperature variance in the interfacial layer depends on its stability and the entrainment heat flux, both being functions of the Froude number (Wyngaard 1985). Therefore, we conclude that the smaller variance in the experiment originates from the larger Froude number, which amounts to 0.32

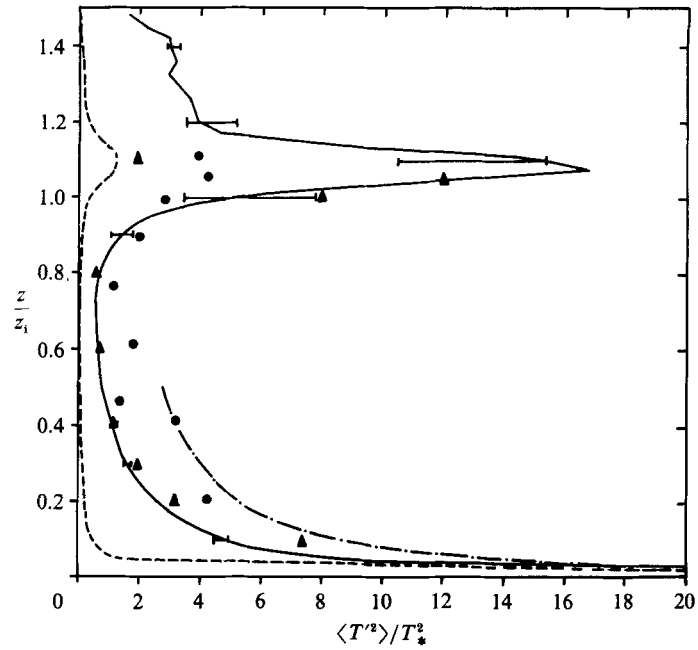

FIGURE 5. Temperature variance versus height. Curves and symbols as in figure 3 except for –·–·–, which represents the interpolation curve $\langle T'^2 \rangle / T_*^2 = 1.8(z/z_i)^{-\frac{2}{3}}$ proposed by Kaimal *et al.* (1976) based on field measurements.

in the experiment while it is 0.0922 in the LES. Our larger temperature fluctuations are not unrealistic: Caughey & Palmer (1979) report a maximum value of about 50 for the normalized temperature variance and Lenschow *et al.* (1980) occasionally find maximum values exceeding 100. Finally, the LES results are close to results of SOC models as reported by André *et al.* (1978) and Finger & Schmidt (1986).

In figure 6, we have plotted the SGS-dissipation rate $\langle \epsilon \rangle$ in comparison with various previous results. We find very good agreement with the LES-result of Deardorff (1974) and the few data points of Deardorff & Willis (1985). However, the present result is much smaller than dissipation profiles observed in the atmosphere by several authors (Caughey & Palmer 1979; Lenschow *et al.* 1980; Druilhet *et al.* 1983; Guillemet, Isaka & Mascart 1983). On the other hand, in the case of strictly zero mean wind, the vertical integral of the dissipation rate must be less than the integrated production rate due to buoyancy because a small amount of energy is consumed by the entrainment process at the inversion. The non-dimensional integral of the dissipation rate amounts to 0.352 ± 0.01, while that of the buoyancy production rate is 0.382 ± 0.01 in our simulations. Hence our results and also those of Deardorff (1974) and Deardorff & Willis (1985) are consistent with this integral balance while the field observations can only be explained by the presence of a considerable fraction of shear production. Thus we conclude that previous results from field observations overestimate the dissipation rate for the CBL with zero mean wind. In fact, Guillemet *et al.* (1983) find that a mean value of 0.35 for the normalized dissipation rate represents a lower limit to atmospheric observations for very small friction velocities.

The triple moment of the vertical velocity fluctuations is shown in figure 7. This curve measures the contributions of the resolved scales only. The triple moment is

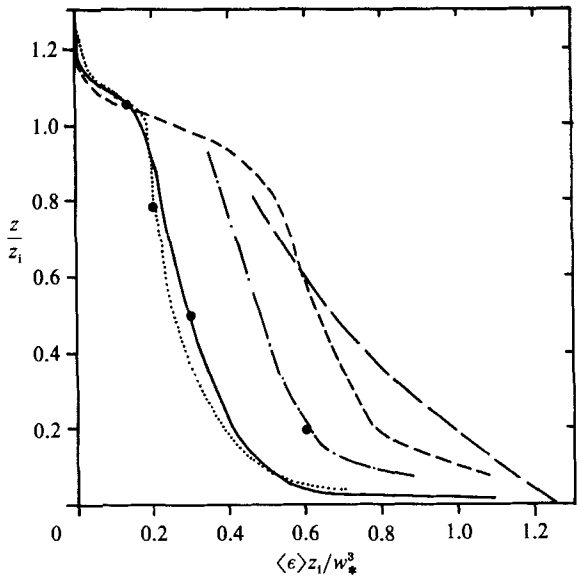

FIGURE 6. Dissipation rate versus height: ——, present LES; · · · · ·, LES of Deardorff (1974); – – – –, mean value of field observations by Caughey & Palmer (1979); — —, aircraft measurements by Druilhet *et al.* (1983); —·—·—, aircraft measurements by Lenschow *et al.* (1980); ●, laboratory measurements by Deardorff & Willis (1985).

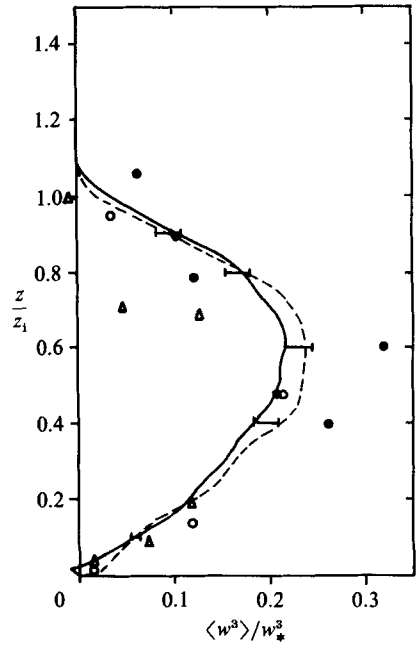

FIGURE 7. Triple correlation of vertical velocity fluctuations versus height (resolved part only). Curves and symbols as in figure 3 except for the dashed curve, which is the LES-result for c_t enlarged by 20% relative to the standard value given in table 1.

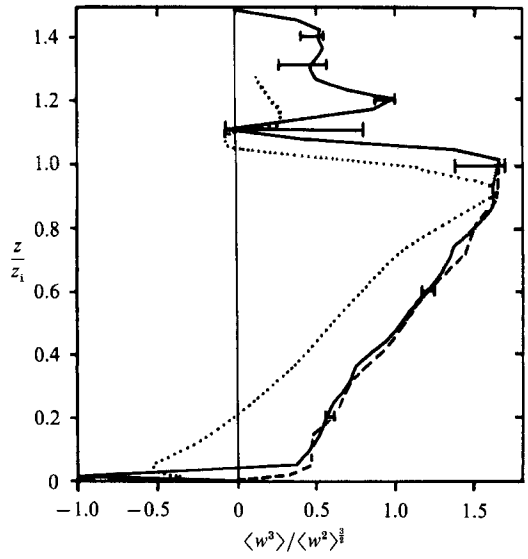

FIGURE 8. Skewness of vertical velocity fluctuations versus height (resolved part only). —— (with error bars), present LES results; · · · · ·, LES result by Deardorff (1974); - - - - -, present LES result for c_l enlarged as in figure 7.

non-zero because of the non-Gaussian, asymmetric flow structure with narrow strong updraughts and wide weak downdraughts. Tower measurements summarized by Hunt *et al.* (1988) indicate that the triple moments increase as $\langle w^3\rangle/w_*^3 = z/z_i$ near the surface and reach a maximum of about 0.25 in the middle of the mixed layer. Our numerical results show, however, a small negative value in the lowest mesh cell. Such negative values imply an unexpected downward transport of kinetic energy. This indicates a problem due either to finite-difference errors or deficiencies in the SGS model. A simulation with $c_l = 1.2c_{\epsilon m}$ instead of $c_l = 1.0c_{\epsilon m}$ does not show this negative value and this indicates that the problem is mainly caused by the SGS model. We shall come back to this point later. Above the first grid cell, the triple moment increases nearly as steeply as predicted by Hunt *et al.* (1988). Thus we can assume that SGS contributions are small. In the mixed layer, the results agree quite well with the measurements of Deardorff & Willis (1985) which obviously exhibit large measurement uncertainties. The aircraft measurements of Lenschow *et al.* (1980) also show quite a large scatter but the mean values do agree with our numerical results.

Figure 8 shows the velocity skewness. The results of Hunt *et al.* (1988) imply a value of about 0.4 in the lower atmosphere. Our numerical results are close to this value near $z \approx 0.1z_i$. In this figure, the problem of negative triple correlation becomes even more obvious than in figure 7. As discussed in Hunt *et al.* (1988), both the LES-results of Deardorff (1974) and those of Moeng (1984) reflect a difficulty in the model in this respect. It should be noted that third-order closure models such as those of Zeman & Lumley (1976) and Chen & Cotton (1983) also suffer from this problem. Even Willis & Deardorff (1974) could not entirely exclude negative triple correlations in their laboratory experiments.

There is little experimental data with which one can compare the results for the pressure fluctuations, see figure 9. Our results agree well with those reported by Deardorff (1974). However, our results are about 40% smaller than those of Moeng

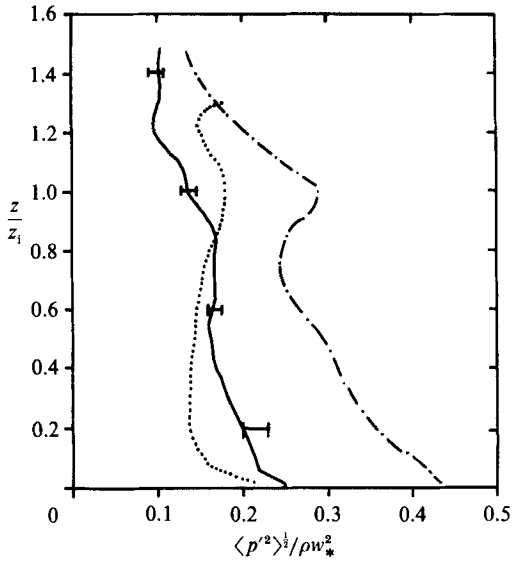

FIGURE 9. R.m.s. value of pressure fluctuations versus height (resolved part only): —— (with error bars), present LES-results; ·····, LES result by Deardorff (1974); –·–·–, LES result by Moeng & Wyngaard (1986).

& Wyngaard (1986). Their simulations show large buoyancy contributions which are particularly large near and above the inversion level. They find good agreement with data deduced from Doppler-radar measurements by Gal-Chen & Kropfli (1984). However the experimental data were obtained for a highly transient CBL with considerable shear above, so that they may not be valid for the present case. C.-H. Moeng (personal communication 1988) found that her pressure profile results were steady for three turnover time units so that numerical disturbances are less likely in causing her large pressure fluctuations. The dotted curve in figure 9 is the result Deardorff (1974) obtained at the final time of his simulation. Results at earlier times show even smaller pressure fluctuations. As time proceeds, he finds that the r.m.s. pressure increases mainly near and above the inversion. This suggests that his simulations may contain spurious oscillations due to gravity waves reflected from the top boundary of the computational domain while this effect is avoided in our scheme, which uses a radiating boundary condition.

In summary, the mean profiles are in sufficient agreement with previous findings to conclude that the simulations give realistic results for the CBL both under laboratory and atmospheric conditions. The unexpected negative velocity-skewness values will be explained in §3.6.

3.2. *Spectra*

Spectra identify the importance of various scales. They are also most sensitive to the SGS-model and can thus be used to validate the parameters of the model (Deardorff 1971). One-dimensional spectra along horizontal lines were obtained by Fourier transforming the fields and averaging over all parallel lines at fixed height and time. The spectra are denoted by Φ_w, Φ_u and Φ_T for vertical velocity, horizontal velocity, and temperature, respectively. They are functions of discrete horizontal wavenumbers k which are multiples of $2\pi/X$. As in Deardorff & Willis (1985), the spectra are multiplied by the wavenumber and normalized by the convective scales and then

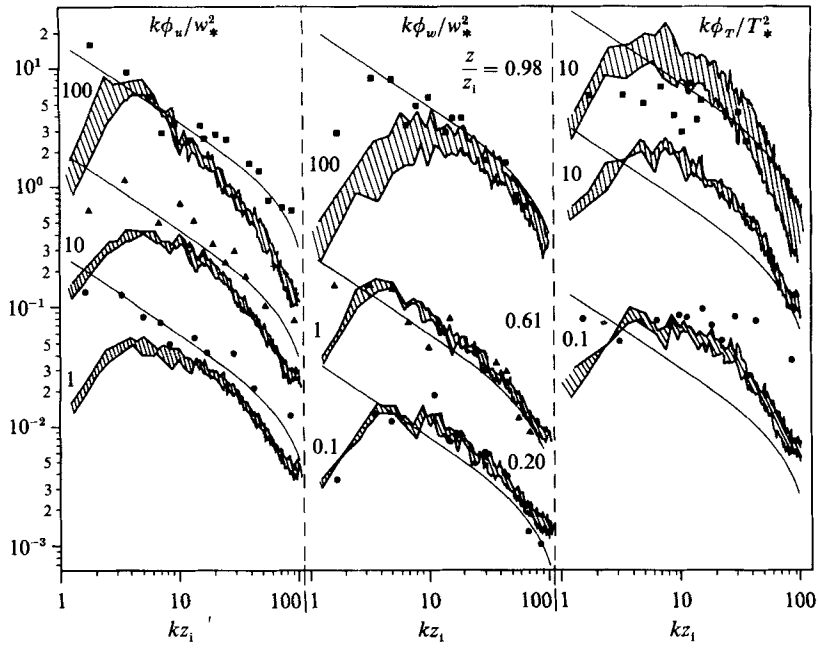

FIGURE 10. Normalized horizontal spectra of horizontal velocity Φ_u, vertical velocity Φ_w, and temperature Φ_T, multiplied by the horizontal wavenumber k, versus normalized horizontal wavenumber kz_i at heights $z/z_i = 0.20, 0.61$ and 0.98. The data have been multiplied by the decimal factors as given in order to avoid overlap, e.g. $k\Phi_u/w_*^2$ has been enlarged by a factor of 100 before plotting. The hatched areas represent the range of LES results at times $t_* = 6$, 6.5, and 7. The symbols represent measurements by Deardorff & Willis (1985) at various heights. The thin curves depict the inertia–convective range spectra for filtered data as defined in (14) and (15).

plotted versus kz_i as shown in figure 10. In the inertial subrange one expects Kolmogorov's spectrum, i.e.

$$\Phi_u(k) = \alpha_1 \langle\epsilon\rangle^{\frac{2}{3}} k^{-\frac{5}{3}}, \quad \Phi_w(k) = \frac{4}{3}\alpha_1 \langle\epsilon\rangle^{\frac{2}{3}} k^{-\frac{5}{3}}, \quad \Phi_T(k) = \beta_1 \langle\epsilon_T\rangle \langle\epsilon\rangle^{-\frac{1}{3}} k^{-\frac{5}{3}}, \tag{14}$$

where, according to e.g. Andreas (1987), $\alpha_1 \approx 0.52$, $\beta_1 \approx 0.8$. The dissipation rates of kinetic energy and half the temperature variance are $\epsilon = c_{\epsilon m} \overline{E''^{\frac{3}{2}}}/l$ and $\epsilon_T = \frac{1}{2} c_{\epsilon T} \overline{E''^{\frac{1}{2}} T''^2}/l$, respectively (see Appendix B).

As discussed by Deardorff (1971), one should, however, not expect to see these spectra in finite-difference simulations up to the shortest resolved scales because the discrete grid-point values effectively represent mean values over the grid interval Δx. For such mean values the spectra have to be multiplied by a filter function $F(k)$,

$$F(k) = \left[\frac{\sin(k\Delta x/2)}{k\Delta x/2}\right]^2. \tag{15}$$

Actually, this filter applies to one-dimensional signals. For three-dimensional fields more complicated filters apply (Moeng & Wyngaard 1988) but the given filter should suffice for the present discussion. A strict agreement between the numerical simulations and the theoretical predictions can only be expected when the resolution is fine enough that it truly resolves at least a significant portion of the large-scale end of the inertia range. Otherwise, the spectrum of the numerical results will be

strongly influenced by both the large-scale structure and by the finite-difference approximations. In the present simulation the resolution is still at the lower limit of what is strictly required. Thus, we cannot expect strong conclusions from disagreements in the spectra but they are certainly informative and agreement is a strong indicator for the correctness of the overall model.

In figure 10, the filtered inertial-range spectra are plotted for various heights together with the numerical results and unfiltered data as obtained by Deardorff & Willis (1985). The spectra are not smooth. At low wavenumbers this can be due either to coherent structures as discussed by Grossman (1982) or to statistical errors. Near the inversion, part of the scatter originates from strong height dependence of the spectra and uncertainties in the exact value of z_i. The error bands obtained by comparing the spectra at various times indicate that most of the scatter is of a random nature. A systematic time trend has not been found in the spectra for the time interval $6 \leqslant t_* \leqslant 7$, so that we can be sure that these spectra represent the asymptotic state of the CBL. Besides random variations, some of the peaks and dips in the spectra persist and may reflect large-scale structures. This is the case in particular for Φ_w at $z/z_i = 0.2$. Here, we observe two peaks near $kz_i = 3$ and $kz_i = 9$ corresponding to wavelengths of the order $2z_i$ and $0.7z_i$. As we shall see, these wavelengths are in fact related to the mean distance between plumes and the average diameter of updraughts respectively. These results corroborate Grossman (1982) who concluded that such peaks are realistic. In contrast, Deardorff & Willis (1985) doubt that such peaks have any physical meaning although their experimental spectra show similar ones.

At high wavenumbers, the numerical results decrease slightly more steeply than the theoretical prediction. If the SGS model provides too little damping then this should show as an increase of energy at the highest wavenumber. Obviously, except perhaps for Φ_u at the lowest z-level, this is not the case in these simulations so that we can safely assume that the SGS viscosity is large enough to damp out small-scale fluctuations. In fact, it appears that the damping is perhaps somewhat too large. The spectra show high degrees of anisotropy even at large wavenumbers. The u-spectra are consistently below and the w-spectra for $z/z_i \leqslant 0.61$ are above the theoretical estimates. Also Deardorff (1971, 1972) found in his LES that the ratio of vertical to horizontal velocity spectra far exceeds the theoretical values of 4/3 (by up to a factor 2.6). It appears, that the isotropizing effect of pressure fluctuations is not large enough, for the present range of wavenumbers, to create locally isotropic turbulence. The general level of the velocity spectra agrees approximately with the inertial-subrange theory. The numerical results for the temperature spectra are, however, always above the theoretical predictions. Also the laboratory data show higher values of the temperature spectra (for $z/z_i \leqslant 0.61$) than the inertial-range prediction. Thus, it cannot be known whether the differences are due to errors in our numerical simulations or due to limitations in the applicability of the inertia-range predictions for this situation.

The spectra agree generally with the data of Deardorff & Willis (1985) but some differences are noteworthy. We get poor agreement near the inversion, but this is not surprising as we observed large differences in the mean values at this level which are explainable at least partly by the differences in the Froude numbers as discussed above. For $z/z_i \leqslant 0.61$, the experimental results generally exhibit larger amplitudes at low wavenumbers, in particular with respect to the u-component. As discussed above, we assume that at least part of these differences is due to large-scale inhomogeneities of the surface heating in the experiment.

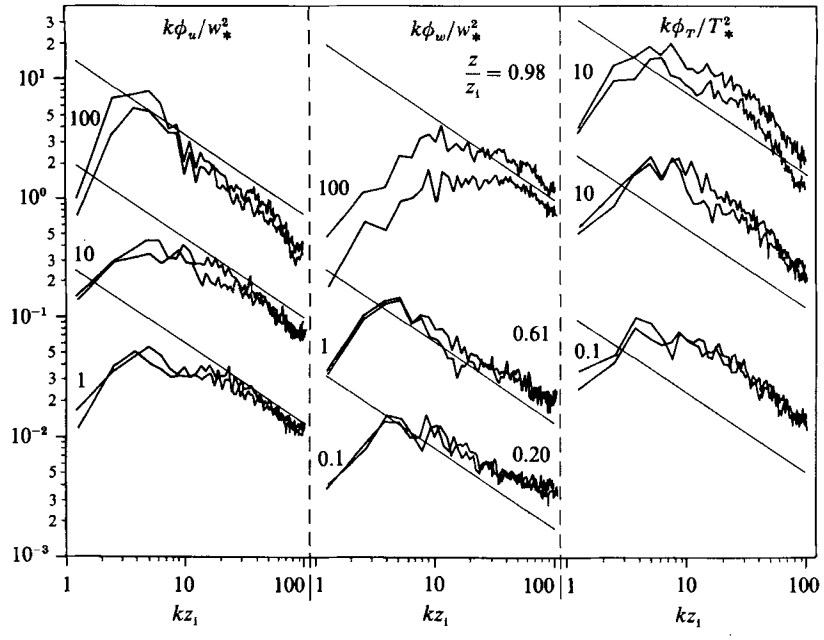

FIGURE 11. Normalized horizontal spectra as in figure 10 but for reduced SGS diffusivities. The full curves represent the LES-results at times $t_* = 6.5$ and 7. The thin curves represent the inertia–convective range spectra for unfiltered data as defined in (14).

In order to test the sensitivity of the computed spectra with respect to the model's coefficients, we have performed a simulation with c_{Rm} and c_{RT} both enlarged by a factor of 1.5. As discussed in Appendix B, the increased coefficients cause reduced SGS diffusivities and thus reduced damping. Since such simulations are very expensive, we have rerun the simulation, starting from the results at $t_* = 6$, and performed the integration over 400 time steps until $t_* = 7$. The resultant spectra are shown in figure 11. As expected, the spectra now agree better with an unfiltered $-5/3$ law but the differences between the u- and w-spectra are reduced only slightly. This confirms that the isotropizing effect of pressure fluctuations does not suffice to reach local isotropy at these scales. The tendency of energy accumulation at the highest wavenumber is still small but obviously enhanced so that these simulations are at the limit of reasonably resolving LES. As can be seen from the spectral results, the low-wavenumber contributions are changed only a little and for this reason all the mean profiles discussed in §3.1 are affected little. It is difficult to decide which results are better. In any case, the results with the original set of coefficient values are in reasonable agreement with measurements and do not exhibit obvious effects from numerical finite-difference errors due to large small-scale fluctuations. Therefore, we shall continue to discuss the results with the original set of coefficient values, except as noted below.

Insight into the structure of the CBL can be obtained from the spectra of the vertical heat flux (cospectra between vertical velocity and temperature fluctuations) shown in figure 12. Note that these results are plotted in linear scales. The general shape of the spectra is as reported by Kaimal *et al.* (1976). Our results are again not smooth but the scatter of the experimental data is even larger. The spectra exhibit large amplitudes over a wide range of wavenumbers at low heights where the vertical heat flux is largest. Thus, as expected, small-scale motions carry the heat upwards

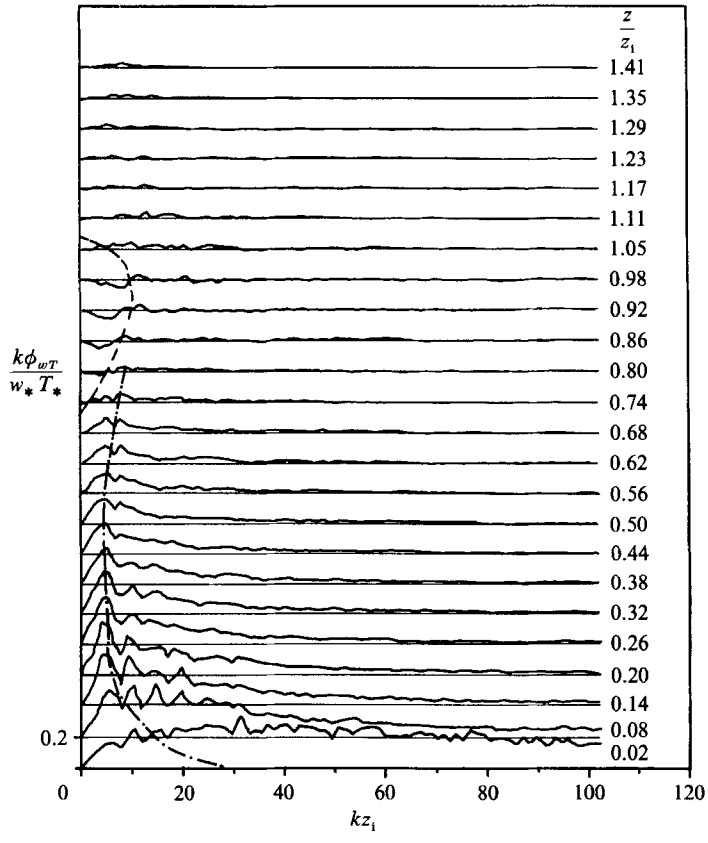

FIGURE 12. Normalized horizontal cospectra of vertical velocity and temperature fluctations ('heat-flux spectra') versus normalized wavenumber kz_i in linear scales for various heights z/z_i at time $t_* = 7$. A multiple of 0.2 has been added to the spectra to separate the curves for various heights. ----, encircles the range of downward heat flux; –·–·– connects the wavenumber values of spectral maxima (note that the spectra are multiplied by the wavenumber k).

near the surface. With increasing height, the amplitude and the width of the heat-flux spectra decrease. The normalized heat-flux spectra take their maxima near a wavenumber of about 5 so that lengthscales of the order z_i are carrying most of the vertical heat flux. As the plotted spectra are multiplied by k, the absolute maximum occurs at even smaller wavenumbers or larger scales. In the interval $0.7 < z/z_i < 1.1$ we find negative heat-flux contributions. Obviously, the negative heat flux is carried solely by the small wavenumber or large-scale motions in the form of cold updraughts and warm downdraughts (Wilczak & Businger 1983) at scales of the order z_i. The large-scale heat flux is already negative at levels where the total heat flux is still positive. At $z/z_i = 1.11$ and above, we find small but significantly positive heat-flux values.

The importance of large scales for the entrainment heat flux has also been observed experimentally by Mahrt & Paumier (1984) and in previous studies cited therein. The fact that entrainment is not a small-scale feature has implications with respect to entrainment models. The spectra clearly show that the vertical heat flux is positive and decays to zero at the inversion for high wavenumbers. Hence, the SGS model should give zero or slightly positive values at this level. However, our SGS model predicts small negative heat-flux values. By reference to (A 10) and (A 6) in

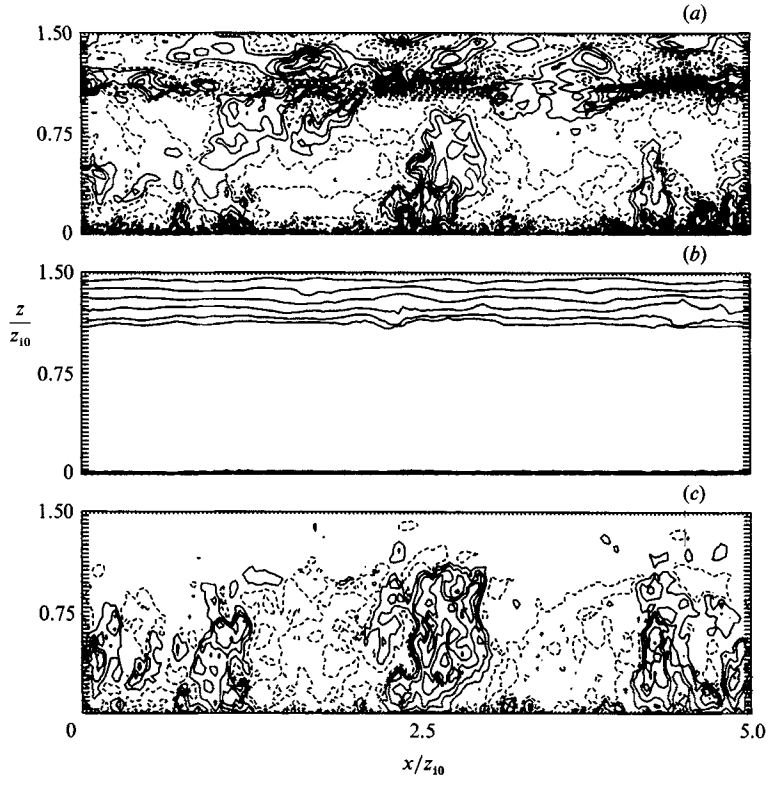

FIGURE 13. Contour plots of (*a*) temperature fluctuations T'/T_{*0}, (*b*) absolute temperature T/T_{*0}, and (*c*) vertical velocity w/w_{*0} for x/z_{i0} versus z/z_{i0} at time $t_* = 7$ in a vertical plane ($y/z_{i0} = 2.437$). The temperature contours apply for $T'/T_{*0} = \pm 0.5, \pm 1.5, \pm 2.5, \ldots$ and those of velocity for $w/w_{*0} = \pm 0.2, \pm 0.6, \pm 1.0, \ldots$. Dashed curves represent negative velocity values. The contour line increment of absolute temperature is $\Delta T = 8T_{*0}$.

Appendix A we see that this suggests that the value of the coefficient c_{BT} is too large. This coefficient accounts for the redistributing effects of pressure fluctuations linearly correlated with buoyancy forces. In the present simulations, with rather high resolution, this SGS contribution is negligible but it might be important otherwise and demonstrates the necessity for a SOC model.

3.3. *Instantaneous fields*

We now turn to the spatial structure of the turbulent velocity and temperature fields. Figures 13 and 14 show contour plots of the fields of vertical velocity and of temperature in vertical and in horizontal cross-sections at various heights at the final time of our simulation. Plots for $t_* = 6$ show similar patterns. Figure 13 has been selected from a series of parallel vertical sections to identify single updraughts. The selected section shows clearly the existence of strong and narrow updraughts, some of which extend over the whole CBL. Often the strong updraughts have well-defined edges with step-like variations of velocity and temperature as observed in the atmosphere (Kaimal *et al.* 1976; Lenschow & Stephens 1980). Both, the velocity and temperature contours show several local maxima which suggest that the updraughts contain smaller scale bubbles. A computer movie generated from a sequence of such plots shows that the bubbles are rising more quickly than the average updraught. The updraughts penetrate into the stable layer which causes an upwelling of the

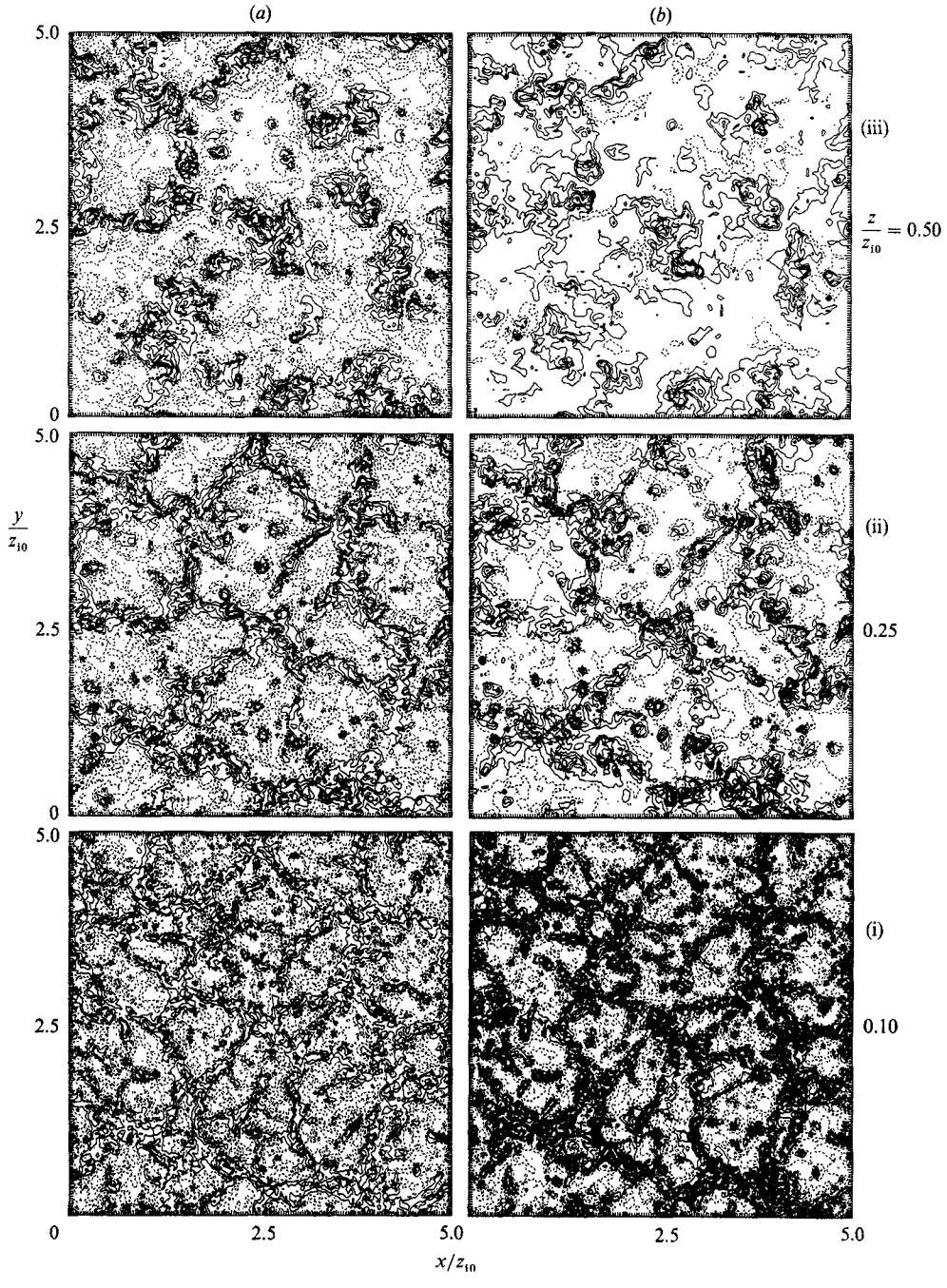

FIGURE 14 (*a*, *b*) (i)–(iii). For caption see facing page.

contours of constant absolute temperature. At the sides of these penetrations, at times when the velocity has already become negative, tongues of warm air, called 'wisps' by Stull (1973), which are best seen from the isothermals of temperature fluctuations, are torn downwards. Such wisps are clearly visible in radar and sodar soundings reported by Rowland & Arnold (1975). Above the inversion there are still

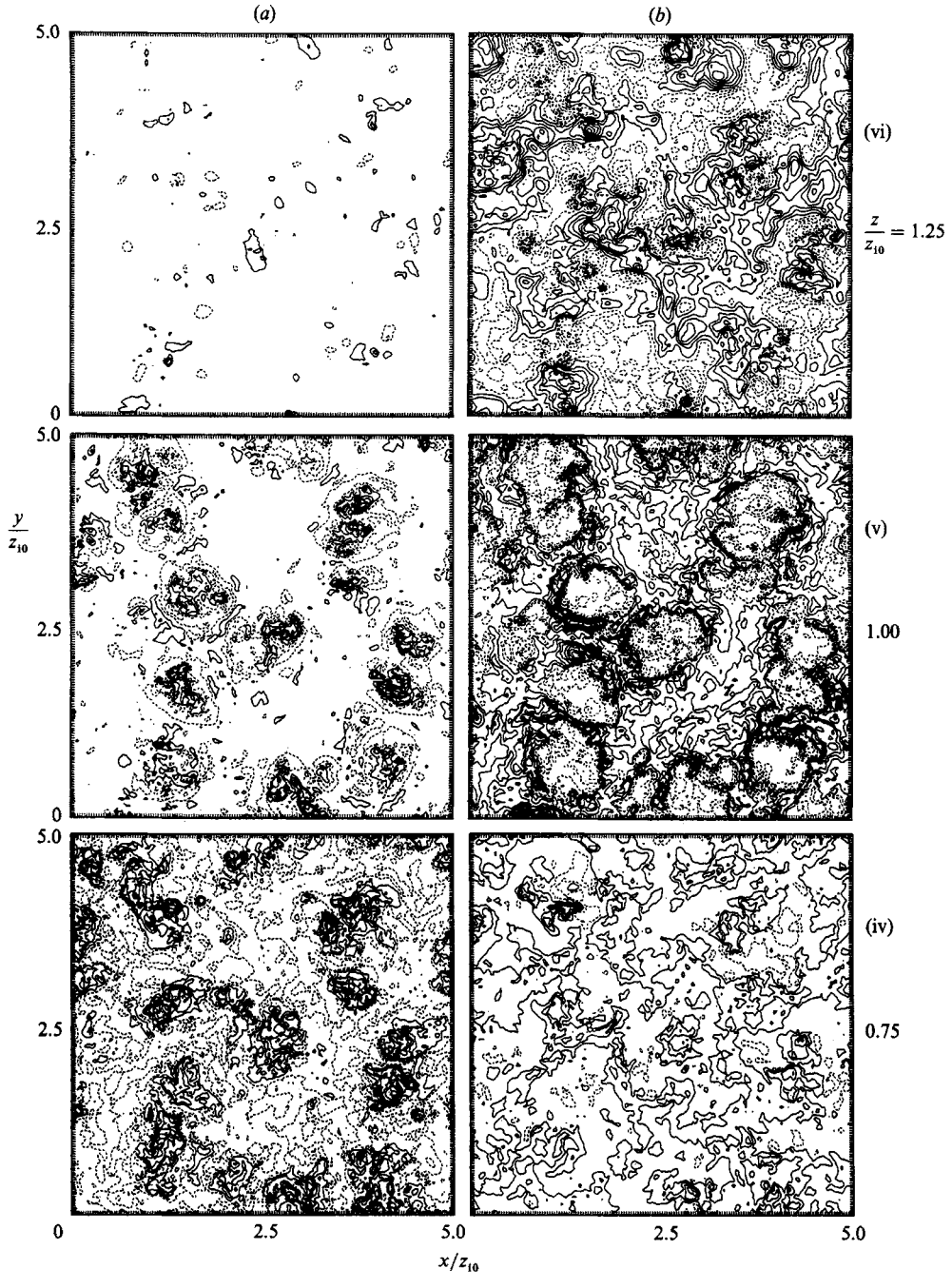

FIGURE 14. Contour plots (a) of vertical velocity w/w_{*0} and (b) temperature fluctuations T'/T_{*0} at time $t_* = 7$ in (x, y)-planes for heights, (i) $z/z_{i0} = 0.097$, (ii) 0.25, (iii) 0.5, (iv) 0.75, (v) 1.00, (vi) 1.25. The contour lines correspond to $T'/T_{*0} = 0, \pm 1, \pm 2, \ldots$ and $w/w_{*0} = \pm 0.2, \pm 0.6, \pm 1.0, \ldots$. Dashed curves represent negative contour values.

considerable temperature fluctuations due to wavy motions. These waves are excited by the updraughts which 'bounce' against the stable layer. Near the surface we see very fine-scaled vertical motion. Small plumes with temperature excess rise from the surface into the mixed layer.

The horizontal cross-sections in the upper mixed layer, figure 14(iv)–(vi), show several isolated plumes with strong updraughts. The typical spacing between these updraughts varies between 1 and $2z_i$. The plumes are seldom round but are very irregular in cross-section. Our results are supported by Lidar observations of Crum *et al.* (1987) who observed a highly convoluted and turbulent outer boundary of thermals which they call 'intromission zone'. Between the updraughts the fluid is sinking while its temperature remains quite uniform. Temperature contrasts are very small at intermediate levels, $z/z_i = 0.5$ and 0.75 (as to be expected from figure 5). At the inversion, we observe that the thermals penetrate upwards in small areas. These areas are surrounded by a ring of downward motions in which the temperature fluctuations are positive. The velocity contours at $z = z_i$ even occasionally show a second ring with upward motion indicating a wave-like spreading of the disturbance radially away from the centre of the upward motion as if a stone had been thrown into a lake. Above the inversion, at $z = 1.25z_i$, the temperature fluctuations indicate large-scale variations. It is clear that small vertical-motion amplitudes would suffice to create large amplitudes of temperature fluctuations in the stable environment. However, the temperature fluctuations are not strongly correlated to the vertical velocity. On the contrary, the velocity fluctuations are small at this level and randomly distributed. The weak correlation is also documented by the small vertical heat flux, see figure 2, at these levels. Small-scale temperature fluctuations dissipate quickly while large-scale fluctuations decay slowly. Thus it is more likely that the temperature fluctuations are remainders of previous excitation by vertical motions and are passive (fossil turbulence) rather than an immediate consequence of actual velocity fluctuations. We have observed similar effects in direct simulations of stratified homogeneous turbulence (Gerz, Schumann & Elghobashi 1989). As explained in Schumann (1987), the large temperature variance in the stable layer represents a reservoir of potential energy $\frac{1}{2}\rho\beta g\langle T'^2\rangle(\mathrm{d}\langle T\rangle/\mathrm{d}z)^{-1}$ which is converted into kinetic energy by the countergradient heat flux. In fact figures 2 and 12 show small but finite values of positive heat-flux values in this domain where the temperature gradient should induce negative heat-flux values.

At smaller heights, figure 14(i)–(iii) exhibits a significantly different flow structure. Convection is organized in lines that are approximately straight and form polygonals. The typical length of the line segments and their horizontal spacing is about $1.3z_i$. If one considers the cross-point of the lines as the axis or the hub of a wheel then the lines look like spokes of a wheel. For this reason this type of structure was called a 'spoke pattern' by Busse & Whitehead (1974). Three or four (occasionally five) spokes join into one hub. From top to bottom, the spoke pattern is observed first in the velocity contours at $z/z_i = 0.5$. The temperature fluctuations are still small at this level and more irregular. With decreasing height, the spoke pattern becomes more and more pronounced and the velocity and temperature fields more strongly correlated (as required for vertical heat flux). Obviously the large-scale updraughts in the upper part of the mixed layer originate at the hubs of the spoke-pattern wheels. As revealed by additional plots in terms of horizontal velocity in horizontal planes (see also Mason 1987), the vertical motion in the wheel axis is fed by horizontal motion near the surface, first towards the spokes and then inside the spokes towards the hubs. At normalized heights between 0.2 and 0.5, the flow is less regular and

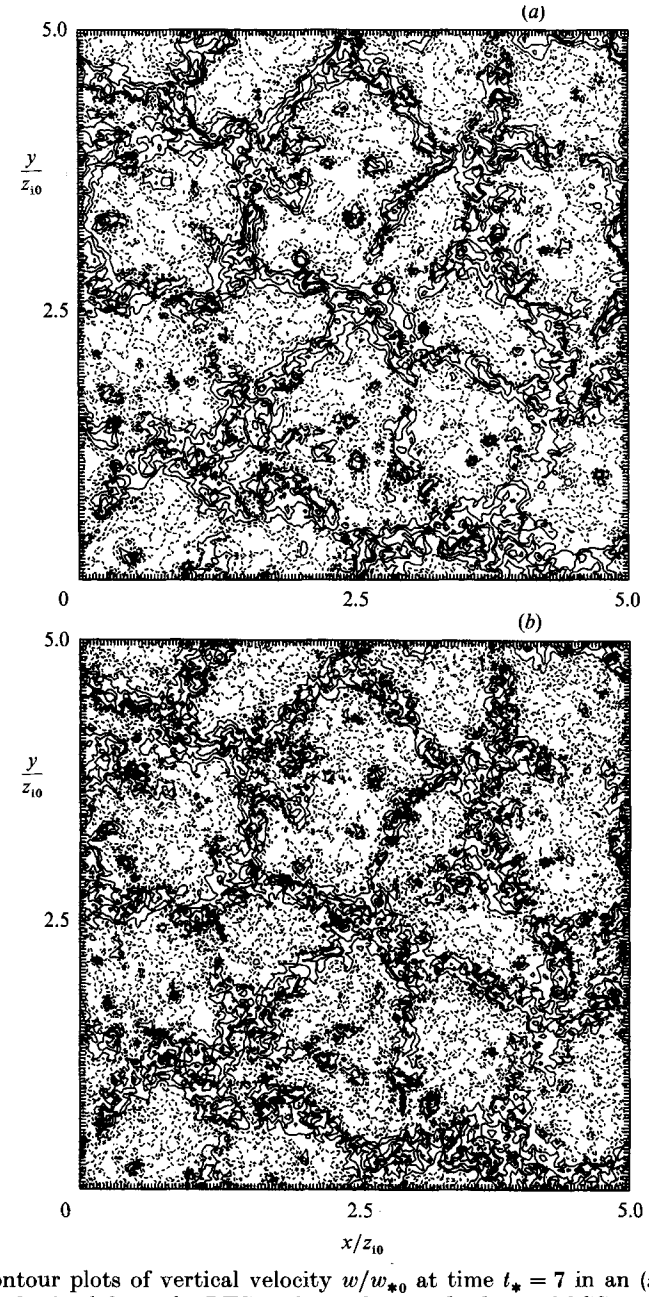

FIGURE 15. Contour plots of vertical velocity w/w_{*0} at time $t_* = 7$ in an (x, y) plane for height $z/z_{i0} = 0.25$ as obtained from the LES with (*a*) the standard set of SGS coefficients and (*b*) with reduced SGS diffusivities. The contour lines are coded as in figure 14.

occasionally spirals with some vertical vorticity into the updraughts. At $z/z_i = 0.25$ and below, we observe several small spots inside the downdraughts. Obviously only those small-scale plumes that are close to a hub merge into the updraught while small-scale thermals in the downdraught area arise from the surface and propagate a small distance upwards but then decay.

In figure 15 we show that the spoke pattern persists in the simulations if the SGS diffusivity is reduced. This figure shows one horizontal cross-section of the vertical

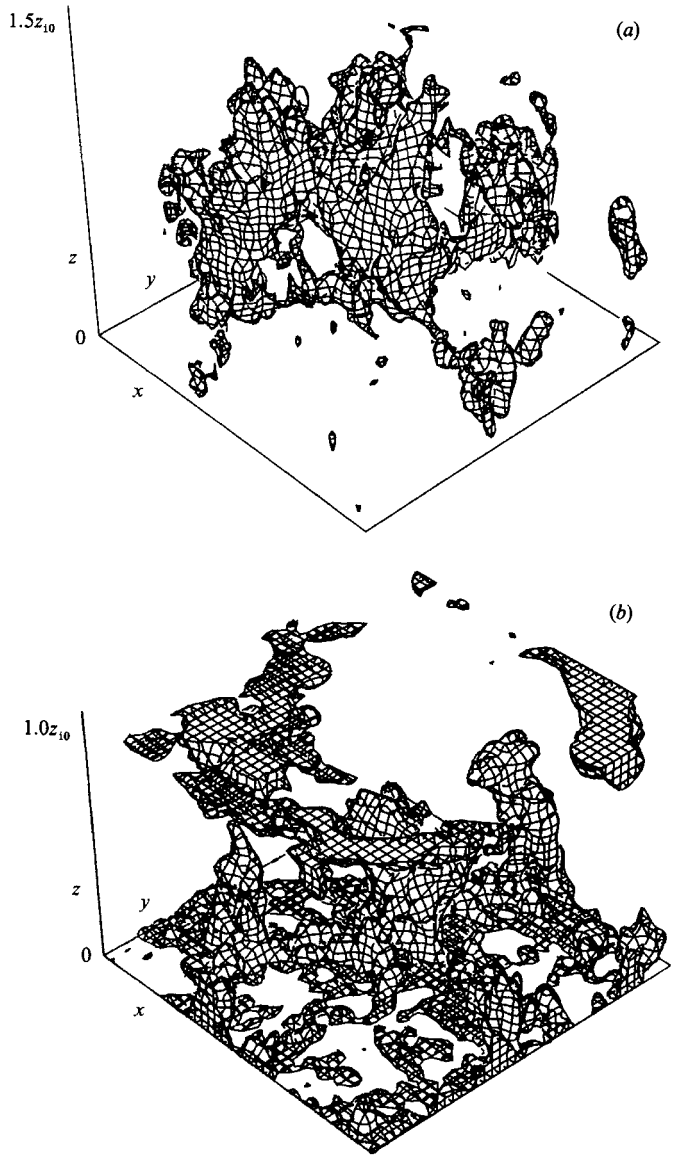

FIGURE 16(*a*). Perspective view of the surface of constant vertical velocity $w/w_{*0} = 1.0$ at time $t_* = 7$. Inside the surface the velocity is larger than on the surface. The data are from a sub-volume of the simulation results comprising $0.906 \leqslant x/z_{i0} \leqslant 2.125$, $2.22 \leqslant y/z_{i0} \leqslant 3.44$, $0 \leqslant z/z_{i0} \leqslant 1.5$. The point of view is at $(x, y, z)/z_{i0} = (6.25, -4.375, 6.25)$ relative to the origin shown by the coordinate axis. (*b*) Perspective view of the surface of constant temperature $T/T_{*0} = 660.9$ at time $t_* = 7$. Inside the surface the temperature is higher than on the surface. The data are from a sub-volume of the simulation results comprising the same horizontal section as in (*a*) but extending over a smaller height interval $0 \leqslant z/z_{i0} \leqslant 1.0$. The point of view is the same as in (*a*).

velocity field from both our standard case and the case with 50% increased values of c_{Rm} and c_{RT} for which we have shown spectra in figure 11. This cross-section is representative of all other cross-sections in showing the spoke pattern. Figure 15(*b*) clearly reflects the larger content of small-scale motions for reduced SGS diffusivity but the large-scale spoke pattern still dominates. In fact, (*a*) and (*b*) show more or less

the same large-scale structure not only in the mean but also with respect to individual details. Thus, the large-scale spoke pattern is only weakly dependent on small-scale disturbances.

In figure 16 we present perspective views of surfaces of constant vertical velocity and constant temperature as obtained with the standard set of coefficient values. For this purpose, a subvolume of the whole computational domain has been selected which contains one large updraught in the middle and two further strong updraughts at the sides. The whole computational domain would give too complicated a picture. Figure 16(*a*) clearly illustrates three spokes connecting the centre plume with its neighbours. Obviously, the plumes are not smooth. They are larger in height than in diameter. However, they are much thicker than Hess, Spillane & Lourensz (1988) suggest in a corresponding sketch. The empty area is filled with downdraughts and we observe a few smaller updraughts in this area but they die out while rising. They do not seem to merge together. The temperature surface in figure 16(*b*) again shows one large plume in the centre together with two smaller neighbours. Many small thermals near the surface rise against the downdraughts and then decay. The big plume in the centre has penetrated the inversion and this is reflected by the circular open area of low temperature at the top of this plot which ends at $z/z_i = 1$. This open circular area is surrounded by small warm downdraughts extruding down into the mixed layer. The result shows that part of the entrainment flux is connected with large-scale downward motion along circles around the updraughts but with smaller scale temperature variations. It supports the concept of 'wisps' introduced by Stull (1973) to explain the entrainment flux.

3.4. *Correlation functions*

In order to determine the mean spatial structure of the CBL we compute correlations between vertical velocity $w(x, y, z_c, t)$ at height z_c and any other field function $f(x, y, z, t)$ according to

$$R_{wf}(x, y, z, t, z_c) = \langle w(x', y', z_c, t) f(x'+x, y'+y, z, t) \rangle, \tag{16}$$

where we average over all positions (x', y') in the computational domain. Instead of vertical velocity one could have selected any other field component but vertical velocity best shows the CBL structure. The height z_c defines the 'reference level' and x and y are the horizontal separations from the 'reference point'. The coordinate values $x+x'$ and $y+y'$ are evaluated modulo X according to the periodic boundary conditions. In the windless CBL, the correlation function is symmetric about the axis $x = y = 0$. Thus it cannot provide any information on the spoke pattern. Also, the averaging smoothes out edges of updraughts and small-scale thermals inside updraughts.

Figure 17 shows some of the correlation functions obtained by averaging over the results at times $t_* = 6.0, 6.1, \ldots, 7.0$. As these correlation functions are functions of three space coordinates and involve averages over all points in a horizontal plane, their evaluation requires considerable computing time (35 minutes of CRAY-XMP for each average at a given time). As the results show, the statistical uncertainty induced by the limited data base, which causes for example deviations from symmetry, does not appear to be large. The results depend on the selected reference level (here $z_c = z_i/2$).

In order to interpret the results, we recall that the correlations between w at one point and f at another point at large separation is large if both functions show large turbulent fluctuations and if they are correlated owing to large-scale coherence.

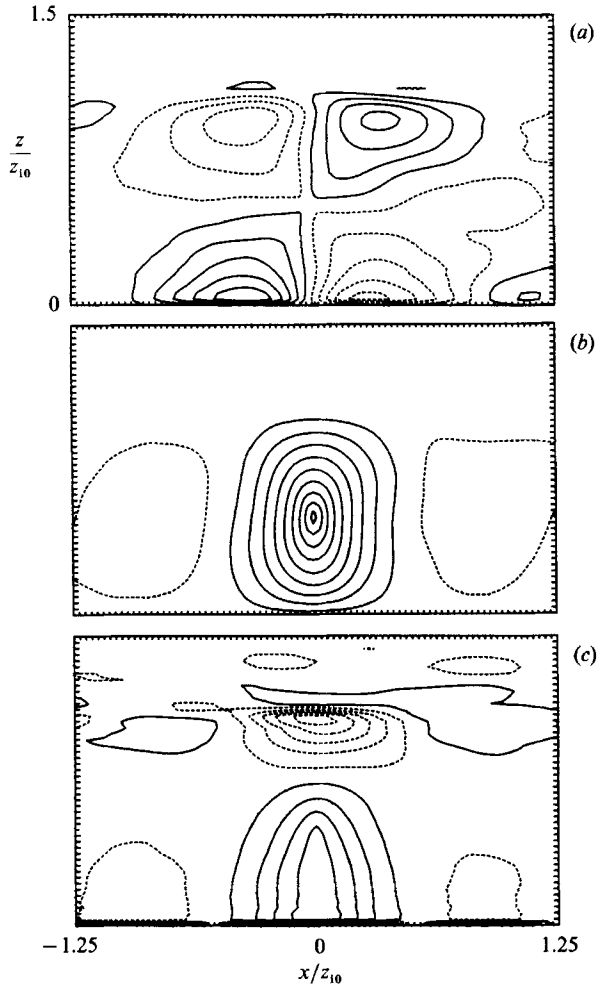

FIGURE 17. Correlation functions (*a*) R_{wu}, (*b*) R_{ww}, and (*c*) $R_{wT'}$, averaged over the time period $6 \leqslant t_* \leqslant 7$ for $z_c = 0.5 z_i$, in a vertical (x, z)-plane, $y = 0$, $0 \leqslant z/z_{i0} \leqslant 1.5$, $-1.25 \leqslant x/z_{i0} \leqslant 1.25$. For larger x-values, the correlation functions are very small and are therefore not shown. The contour-line increments, the minimum and the maximum values are $(0.02, -0.09, 0.1)\, w_*^2$, $(0.04, -0.04, 0.34)\, w_*^2$, $(0.04, -1.26, 0.63)\, w_* T_*$, from (*a*) to (*c*) respectively. In this and the subsequent contour plots, the contour levels are set such that the zero value is excluded for those functions that are not strictly positive (levels $\pm 0.5\Delta, \pm 1.5\Delta, \ldots$ for given increments Δ). Contours for negative levels are dashed.

Moreover, we note that the correlation function averages over both updraughts and downdraughts. Thus, its pattern is not the pattern of updraughts. The horizontal separation between the reference point and the zero contour is a measure for integral lengthscales.

Figure 17 displays the correlations between the velocity components u and w and the temperature fluctuations T' at any point in a vertical plane correlated with the vertical velocity $w(z_c)$ in the same plane, as defined in (16). The correlation functions show coherence from the surface up to the inversion. Horizontal velocity and temperature fluctuations show quite large correlation maxima at large separations. Rising motion in one convective element is correlated with motion towards the foot of this element near the surface and motion away from its head near the inversion.

The temperature fluctuation is positive at the foot of the convective structure (but negative at the surface itself) and negative in the interfacial layer. The result clearly shows the dominance of large-scale circulations. In particular, we note the pronounced maxima of horizontal velocity in the surface layer. The corresponding extrema in the interfacial layer are less pronounced. Thus the average rising or sinking fluid element is connected with horizontal flow near the surface quite remote from the element's axis.

The fact that the temperature plot shows a maximum in the surface layer is a consequence of large temperature fluctuations and large coherence. Such coherence suggests large-scale plumes. In contrast, rising thermals would cause a local temperature maximum near the reference point and little correlation with temperature fluctuations near the surface. The reduced surface temperature indicates enhanced heat transfer due to turbulent motion at the foot of plumes. The negative temperature correlation in the interfacial layer above the point of reference originates from thermals which penetrate into the warmer layer above the inversion but are relatively cool. This is one of the causes of entrainment heat flux.

The correlation $R_{ww}(x=0, y=0, z)$ on the axis is the autocorrelation of vertical velocity as a function of vertical separation for which Hunt (1984) predicted a linear increase with z. The constant spacing between the contour lines along the axis clearly supports this prediction. We have also computed the correlation R_{ww^2} between velocity and velocity variance. Its contour plot (not shown) is similar in shape to that of the correlation between the velocities w themselves but the correlation increases approximately quadratically from the surface to the reference level and the contours are a little more concentrated near the axis of symmetry. The radial lengthscale based on the separation of the zero contour of R_{ww} amounts of $0.49z_i$. For comparison, at $z/z_i = 0.48$, Deardorff & Willis (1985) find zero autocorrelation of the vertical velocity at a radius of $0.56z_i$. In view of the statistical uncertainty of such integral lengthscales (Lenschow & Stankov 1986) this difference is small. The lengthscale in terms of surface-layer temperature is $0.53z_i$. Largest is the radius of the area in which horizontal motion near the surface is correlated with rising motion at the reference point: $0.95z_i$. The mean separation between updraughts and downdraughts, measured in terms of the distance of the position of minimum autocorrelation of vertical velocity relative to the axis of symmetry, is $0.93z_i$.

3.5. *Conditionally averaged updraughts and downdraughts*

The correlation functions cannot distinguish between updraughts and downdraughts. Moreover, the pattern of the correlation functions is not the pattern of the convective circulation and may be misleading. Therefore, we have determined conditional averages, which are defined as follows. Let (x_i, y_i), $i = 1, 2, \ldots, n$, be the horizontal coordinates of a centre of an event in terms of an updraught or a downdraught and $f(x, y, z, t)$ be any component of the flow field. Then the conditional average $\tilde{f}$ is the mean value

$$\tilde{f}(x, y, z, t) = \frac{1}{n} \sum_{i=1}^{n} f(x_i + x, y_i + y, z, t). \tag{17}$$

Note the formal similarity with (16). The coordinate values $x_i + x$ and $y_i + y$ are again evaluated modulo X. The crucial aspect of conditional averaging is the definition of the event's centre, i.e. of (x_i, y_i). We define the event using vertical velocity as 'indicator function'. Accordingly, we shall call the results 'w-events'. We have also considered 'T-events' based on temperature fluctuations as the indicator function. However, the differences (for $z_c \approx z_i/2$) are small and so we do not report details of

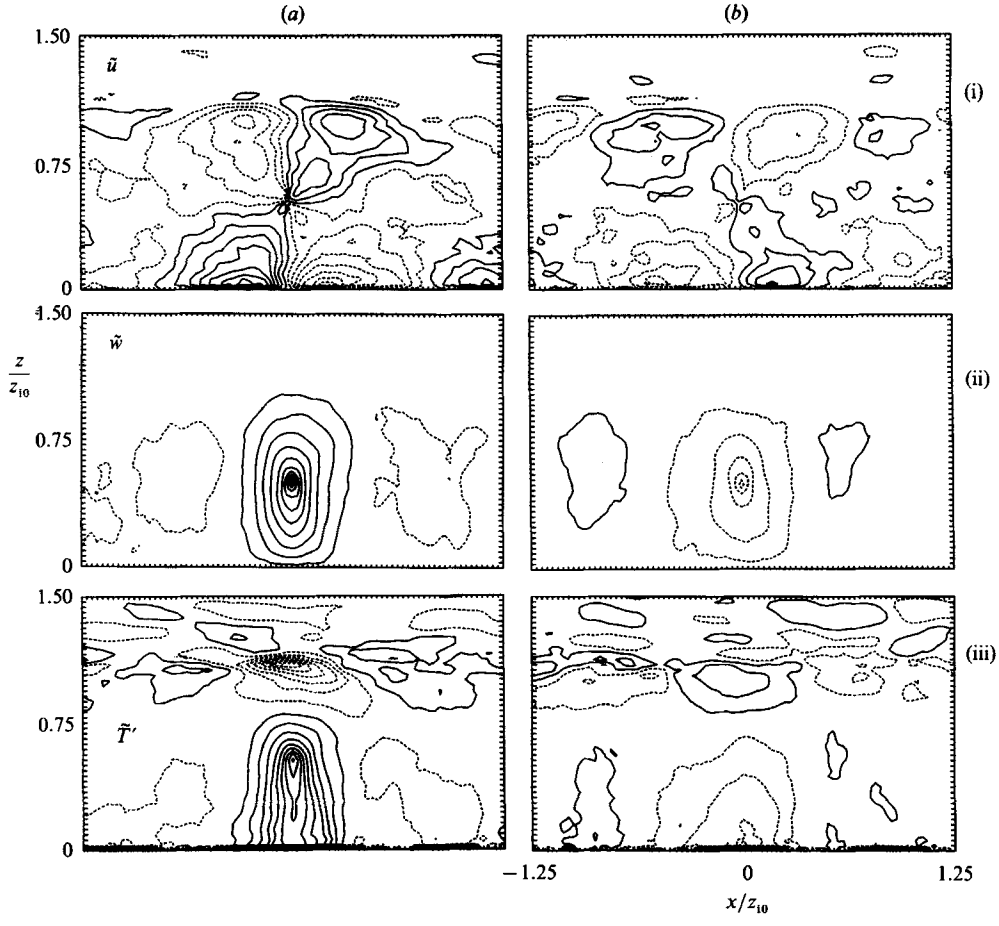

FIGURE 18. Conditionally averaged (*a*) updraughts and (*b*) downdraughts for $z_c = 0.5z_i$ in terms of (i) $\tilde{u}$, (ii) $\tilde{w}$, and (iii) $\tilde{T}$ averaged over the time period $6 \leqslant t_* \leqslant 7$ in a vertical (x, z) plane as in figure 17. The contour-line increments, the minimum and the maximum values of the updraughts and the minimum and the maximum values of the downdraughts are (0.05, −0.36, 0.33, −0.20, 0.18) w_*, (0.2, −0.1, 2.0, −0.96, 0.18) w_*, (0.3, −3.0, 2.7, −3.3, 2.4) T_*, from (i)–(iii) respectively.

such T-events. In either case, the positions (x_i, y_i) are those where the indicator function for $z = z_c$ assumes a local maximum for updraughts (or minimum for downdraughts) of a magnitude exceeding a selected threshold value c and which have a minimum distance d from all other previously found event centres.

The algorithm to determine these positions works as follows. A two-dimensional field of flags is associated with the horizontal grid points. Initially, the flags are set to 'on' and i is set to zero. Then we search for that position where the indicator function assumes the proper extremum (maximum for updraughts) exceeding the threshold value in magnitude. Once this position is found, i is incremented by one and the new position is entered into the actual list of positions (x_i, y_i). Then, for all mesh points which are within a circle of radius d around the actual position, the flags are set to 'off' (including those that are in the circle due to periodicity of the domain). Thereafter, the next position is searched for in the remainder of the domain where the flags are still set to on, etc. The search ends when all flags are set to off or when the resultant extreme-value magnitude no longer exceeds the threshold c.

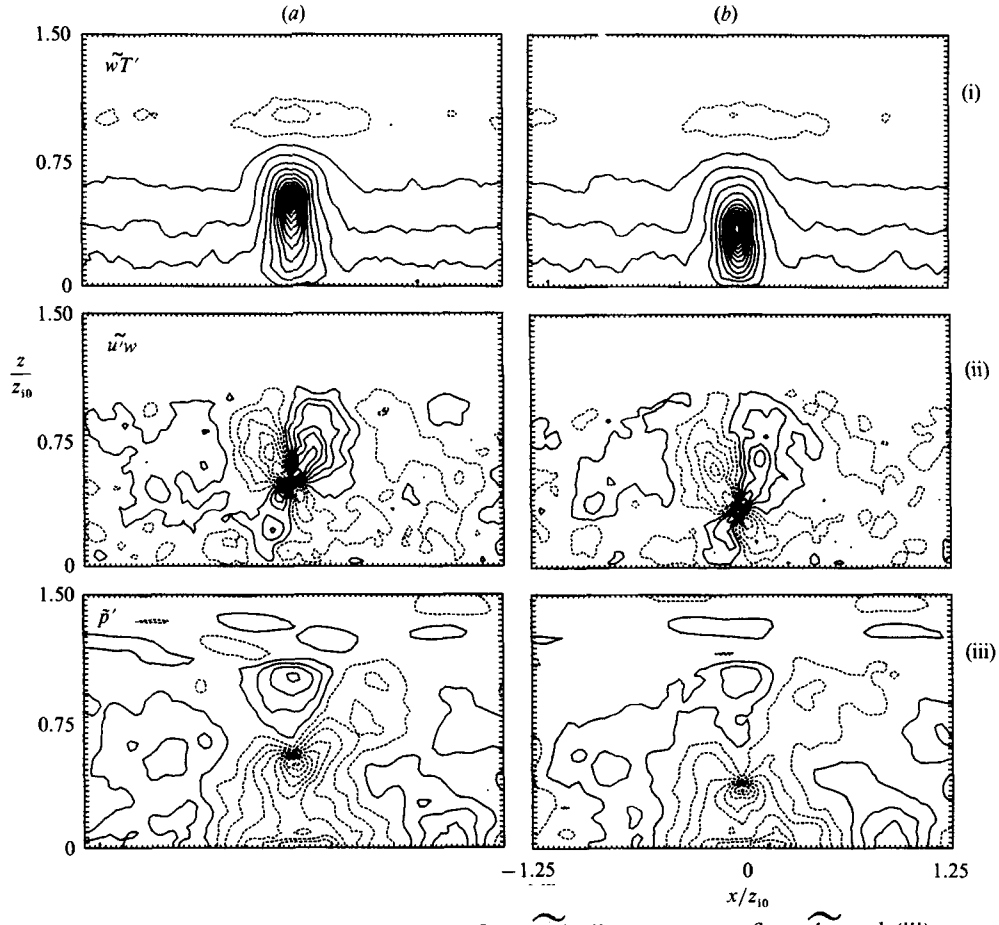

FIGURE 19. Conditionally averaged (i) heat flux $\widetilde{wT'}$, (ii) momentum flux $\widetilde{u'w}$ and (iii) pressure fluctuation $\tilde{p}'$ for (*a*) $z_c = 0.5z_i$ and (*b*) $z_c = 0.333z_i$ for the time period and plane as in figure 18. The contour-line increments, the minimum and the maximum values for (*a*) and the minimum and the maximum values for (*b*) are $(0.3, -0.3, 5.7, -0.3, 6.9)\,w_*T_*$, $(0.02, -0.11, 0.16, -0.13, 0.13)\,w_*^2$, $(0.02, -0.17, 0.07, -0.15, 0.06)\,\rho w_*^2$, from (i)–(iii) respectively.

In general, the results depend strongly on the chosen indicator function, the values of the threshold c, the separation distance d, and the height z_c. If, however, the separation d is selected to be large enough, we average over statistically independent events and the results become insensitive to the actual value of d. They also become insensitive to the threshold c if this value is sufficiently small in comparison with the r.m.s. value of the indicator function, because then the above search loop ends before this threshold becomes effective. This feature is a definite advantage of our method in comparison to other proposals (Lenschow & Stephens 1980; Greenhut & Khalsa 1982, 1987). The dependence on the reference level z_c, however, remains.

Figures 18–20 depict various conditionally averaged fields related to updraughts and downdraughts in terms of contour plots in a vertical plane through the axis of symmetry, we obtained for w-events with a threshold equal to the r.m.s. velocity at the reference level, $c = w'(z_c)$, and $z_c = z_i/2$. The separation distance $d = (X^2/(\pi 8))^{\frac{1}{2}} \approx 1.0z_i$ is constructed such that eight circles of radius d have the same area as the computational domain X^2. However, owing to overlap of the circles, the number of

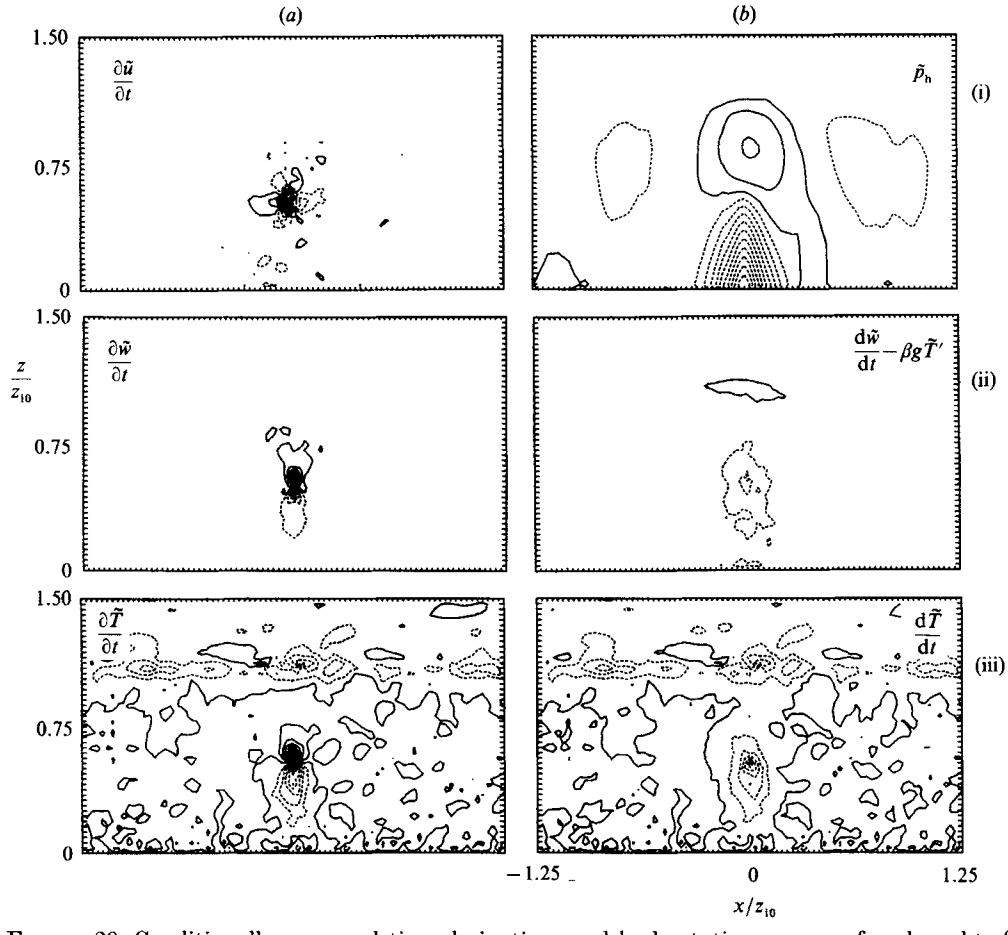

FIGURE 20. Conditionally averaged time derivatives and hydrostatic pressure of updraughts for $z_c = 0.5z_i$ for the time period and plane as in figure 18. (*a*) (i) $\partial\tilde{u}/\partial t$, (ii) $\partial\tilde{w}/\partial t$, (iii) $\partial\tilde{T}/\partial t$. The related contour line increments, the minimum and the maximum values are $(1.0, -5.4, 7.2)w_*^2/z_i$, $(2.0, -20.0, 19.0)w_*^2/z_i$, $(2.0, -16.0, 19.0)T_*w_*/z_i$, from (i) to (iii) respectively. (*b*) shows (i) $\tilde{p}_h$, (ii) $d\tilde{w}/dt - \beta g\tilde{T}$, (iii) $d\tilde{T}/dt$. The related contour-line increments, the minimum and the maximum values are $(0.1, -1.02, 0.24)\rho w_*^2$, $(2.0, -5.1, 2.1)w_*^2/z_i$, $(2.0, -12.6, 5.4)T_*w_*/z_i$ from (i)–(iii) respectively.

events is greater. On average, we find 16 updraughts and downdraughts in the computational domain. For half the separation distance, this number increases to 28. Such halving of the separation distance causes a decrease of the maxima of $\tilde{u}$, $\tilde{w}$, $\tilde{T}'$ and $\widetilde{wT}'$ by 10, 10, 0 and 24%, respectively. The shape of the convective structure remains virtually unchanged and the statistical uncertainty decreases only slightly. Thus the effect of reducing the separation distance is small, and the present results are significant and not a pure function of the selected sampling parameters. The results shown in figures 18–20 represent mean values over 400 time steps from $t_* = 6$ to 7 (with fixed sampling parameters). This long averaging period was necessary to bring the statistical errors down to acceptable levels. If we assume that the lifetime of small-scale thermals is of order 0.1 (in the non-dimensional units) then we average over approximately 160 independent events. Thus the standard deviation of the mean values is of order $160^{-\frac{1}{2}} \approx 0.08$ times the maximum r.m.s. value of the individual fields. Such statistical errors cause the deviations from symmetry which

are noticeable from the plots in figures 18–20. Longer living components of the structure will be even more uncertain and this seems to be the case in particular for the mean pressure, see figure 19.

The results clearly show the existence of large-scale updraughts and downdraughts which extend from the surface up to the inversion. The pattern of the updraughts is in fact similar to that shown by the correlation function. However important differences are to be noted. The conditionally averaged updraughts have large vertical velocity (maximum value $= 2.0w_*$). The horizontal radius is approximately $0.33z_i$. Downdraughts show a minimum velocity of $-0.96w_*$ and a larger radius ($0.5z_i$). The ratio of updraught to downdraught speed amounts to 2.1. This value is considerably larger than the value 1.5 reported by Greenhut & Khalsa (1987) based on a different sampling procedure. Both the updraughts and downdraughts are correlated with strong horizontal velocities (up to $0.36w_*$) in the surface layer. This correlation has also been observed by Coulman (1970). It can also be identified from Doppler-radar observations reported by Frisch *et al.* (1976). The temperature pattern shows a coherent structure which extends from the surface up to the inversion but the temperature shows a maximum near the reference level $z_c = 0.5z_i$, which indicates that the updraughts are to a large extent formed by thermals with small radius of coherence. However, the temperature values are still quite large near the surface and this phenomenon is characteristic for plumes extending from the surface at least up to the reference point. The maximum temperature surplus of the updraughts amounts to $2.7T_*$. This is a quite large value. Lenschow & Stephens (1980) and Greenhut & Khalsa (1987) find that the temperature surplus of updraughts decreases with height and has already become negative above $z/z_i \approx 0.4$. This is obviously an effect of different definitions of conditional sampling and shows that our method is more effective in identifying strongly buoyant updraughts. The updraughts cause negative temperature fluctuations in the interfacial layer ($-1.9T_*$) while the downdraughts are connected with positive temperature fluctuations in this layer ($0.5T_*$). Both effects contribute to the entrainment heat flux (Wilczak & Businger 1983). Above the reference height z_c the motion is away from the updraughts and possesses two maxima of the horizontal velocity, one just above the reference level ($\tilde{u}/w_* = 0.15$) and a second near the inversion ($\tilde{u}/w_* = 0.2$). The first maximum is due to bubbles in the updraughts which displace fluid sideways while rising. The upper maximum reflects the large-scale coherent motion. Note that the results do not preserve the step-wise variations at the boundaries of updraughts or at the inversion layer because of averaging.

Figure 19 shows the fluxes $\widetilde{w\tilde{T}'}$ and $\widetilde{u'w}$ (resolved and SGS contributions) and the dynamic pressure fluctuations $\tilde{p}'$ (resolved part only) connected with updraughts. Figure 19(*a*) shows the results for the reference level $z_c = z_i/2$ as considered in figure 18. For comparison, figure 19(*b*) shows the same functions for a slightly lower reference level. This comparison shows that the results preserve their pattern at least for this variation of the reference level. Significant variations are to be expected, however, if z_c/z_i is taken outside the interval (0.1, 0.8). Updraughts induce large values of upward heat flux which by far exceed the average values. Updraughts are also connected with significant amounts of momentum fluxes. Most of these fluxes are simply due to the product $\tilde{u}\tilde{w}$ but small-scale turbulence (at resolved and subgrid scales) also contributes to these fluxes. Note that the momentum flux is virtually zero at the surface itself. Thus friction at the surface plays a minor role in the dynamics of the updraughts. This result was postulated by Schumann (1988) who assumed that the horizontal motion in the surface layer loses most of its momentum by large-scale

advection across the interface between the surface layer and mixed layer. In fact, the momentum flux is largest above the reference level. Thus the updraughts lose substantial amounts of kinetic energy by momentum flux and shear at the inversion. The pressure signal exhibits considerable statistical uncertainty but it is nevertheless obvious that the pressure is most affected by the large-scale dynamics of the updraughts and the pressure fluctuation is negative below the thermal. This behaviour is to be expected from hydrostatic considerations (see below). Qualitatively the same structure has been found by Wilczak & Businger (1984) from conditionally averaged pressure fields for the surface layer of the CBL. The negative pressure fluctuation just below the point of reference is presumably caused by buoyant bubbles which suck in air from below and from the sides. Pressure fluctuations assume a positive maximum near the inversion presumably because of a pressure head due to thermals impinging on the inversion.

Figure 20 displays fields of time derivatives in updraughts and the related hydrostatic pressure. Both local ($\partial/\partial t$) and Lagrangian time derivatives ($\mathrm{d}/\mathrm{d}t \equiv \partial/\partial t + \tilde{w}\partial/\partial z$) are plotted. The temperature derivatives are most noisy and indicate the limitations of the finite data base. For 'quasi-stationary' updraughts the local time derivatives should be less than unity in the non-dimensional units (timescale greater than z_i/w_*) but we observe much larger local time derivatives. The Lagrangian time derivatives are smaller but still much larger than unity. Lenschow & Stephens (1980) had to assume that local time derivatives were small in their analysis of the vertical momentum balance of updraughts using conditionally averaged flight data. We cannot decide whether their assumption might still be valid for the different sampling definition which they used but our results cast some doubts on this assumption. The present results indicate that updraughts are composed of two types of motion: large-scale quasi-steady circulations together with small-scale rising thermals. The thermals cause large local time derivatives near the point of reference. The acceleration values increase when z_c is decreased. At larger distances from the point of reference, the accelerations are small. The small time-derivatives of horizontal motion in the surface layer confirms the applicability of the Monin–Obukhov relationships for evaluation of surface fluxes. This justifies both our surface boundary conditions and the model used by Schumann (1988). However, updraughts inside the mixed layer are definitely unsteady.

As a crude but simple model, the dynamics of rising thermals may be approximately described by entrainment equations adapted from those given by Turner (1986):

$$\frac{\mathrm{d}\tilde{T}}{\mathrm{d}t} = \frac{\partial \tilde{T}}{\partial t} + \tilde{w}\frac{\partial \tilde{T}}{\partial z} = -3\gamma_T \frac{\tilde{w}}{r}\tilde{T}, \tag{18}$$

$$\frac{\mathrm{d}\tilde{T}}{\mathrm{d}t} = \frac{\partial \tilde{w}}{\partial t} + \tilde{w}\frac{\partial \tilde{w}}{\partial z} = -3\gamma_w \frac{\tilde{w}}{r}\tilde{w} + \beta g\tilde{T}. \tag{19}$$

Here, r is the radius of the thermals as determined from figure 18, and γ_T, γ_w are the entrainment coefficients. These equations are designed for spherical thermals rising in a neutral environment with negligible virtual mass. For $z_c = 0.5z_i$, we obtained $r \approx 0.33z_i$. From the minimum values of the Lagrangian derivatives $\mathrm{d}\tilde{T}/\mathrm{d}t = -12.6T_* w_*/z_i$ and $\mathrm{d}\tilde{w}/\mathrm{d}t - \beta g\tilde{T} = -5.1w_*^2/z_i$ shown in figure 20 and the corresponding values $\tilde{w} \approx 2.0w_*$ and $\tilde{T} \approx 2.7T_*$ we estimate

$$\gamma_T \approx 0.26, \quad \gamma_w \approx 0.14. \tag{20}$$

These values change only little if we halve the separation distance ($\gamma_T = 0.23$, $\gamma_w = 0.15$), or if we reduce the reference level to $z_c = z_i/3$ ($\gamma_T = 0.21$, $\gamma_w = 0.16$). The entrainment-coefficient values are close to common estimates which vary between 0.20 or 0.25 according to Turner (1986). Our results indicate very vigorous small-scale mixing as found by Crum *et al.* (1987), in particular for temperature. The larger entrainment coefficient for temperature is consistent with a smaller value of the turbulent Prandtl number for small-scale mixing, compare equation (B 18) in Appendix B. Further analysis has shown that updraughts are connected with pronounced local maxima of dissipation rate ($1.4w_*^3/z_i$) and SGS kinetic energy ($0.132w_*^2$) at the reference point, which shows the presence of mixing quantitatively. Conversely, downdraughts experience reduced dissipation rates and SGS kinetic energy, so that they are less affected by entrainment.

For stationarily rising thermals, $\mathrm{d}\tilde{w}/\mathrm{d}t = 0$, equation (18) shows that the thermal terminal velocity is

$$\tilde{w} = \left(\frac{\beta g r \tilde{T}}{3\gamma_w}\right)^{\frac{1}{2}}. \tag{21}$$

Hence, as expected, large thermals rise faster than smaller ones. This explains why the flow in the lower mixed layer converges mainly towards the centre of the large updraughts which form at the hubs of the spoke pattern. Also it suggests that adjacent small plumes are drawn into the wake behind the largest thermal.

The hydrostatic pressure in figure 20(*b*)(i) has been obtained from

$$\tilde{p}_h = \tilde{p}(Z) + \int_z^Z \rho\beta g \tilde{T}' \,\mathrm{d}z. \tag{22}$$

The result shows large negative hydrostatic pressure at the surface below the relatively light updraught ($\tilde{p}_h(0,0,0) = -0.9pw_*^2$). For comparison the actual pressure field $\tilde{p}'$ connected with the updraught, see figure 20, is much smaller in amplitude (factor 6.7) and different in shape. Thus, hydrostatic pressure is a poor estimate for the actual pressure in the CBL. This was not expected in view of the study of Moeng & Wyngaard (1986) who found that about 40% of the pressure fluctuations are of a hydrostatic nature. A similar difference has also been noted in discussing figure 9. Obviously, the main portion of buoyancy forces is balanced by inertia forces and entrainment drag rather than by pressure. However, the actual pressure fluctuations and the hydrostatic pressure both have a tendency to drive horizontal motions from the foot of downdraughts towards the foot of updraughts as assumed in the model of Schumann (1988). The smaller pressure forces are balanced by smaller momentum fluxes. In fact, figure 19 shows that the momentum flux $\widetilde{u'w}$ is very small at the bottom and still small at the top of the surface layer at $z = 0.1z_i$.

3.6. *Influence of surface roughness*

As explained in the introduction, the present study was initiated by the question of how surface roughness influences the minimum friction velocity and the heat transfer at the surface. The concept of minimum friction velocity was introduced by Businger (1973). Note that the friction velocity is zero in the ensemble mean. We define the minimum friction velocity $\tilde{u}_*$ as the r.m.s. value of friction velocity at the surface for zero mean wind. The heat transfer is measured in terms of the difference $\Delta\theta$ between the mean temperature θ_s at the surface ($z = z_0$) and $\theta_m = \langle T(0.1z_i)\rangle$ at the top of the surface layer (see figure 1). Both values are computable from the LES where local

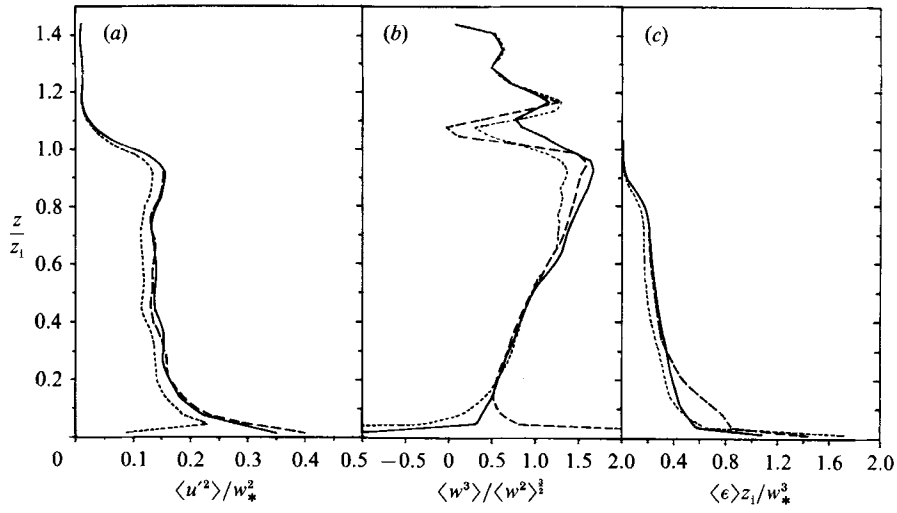

FIGURE 21. Influence of surface friction height z_0 on (*a*) the vertical profile of the horizontal velocity variance (the solid line corresponds to the reference case of figure 4), (*b*) the skewness $\langle w^3\rangle/\langle w^2\rangle^{\frac{3}{2}}$ of vertical velocity (compare figure 8 for the reference case), (*c*) the dissipation rate $\langle\epsilon\rangle$ (compare figure 6 for the reference case): -----, $z_0/z_i = 10^{-2}$, ——, $z_0/z_i = 10^{-4}$; – – –, $z_0/z_i = 10^{-6}$.

values of friction and temperature differences are computed by locally applying the Monin–Obukhov relationships. Schumann (1988) found that these quantities are smooth functions of $\ln(z_i/z_0)$ and approximately equal to

$$\frac{\tilde{u}_*}{w_*} = 0.52\left(\frac{z_0}{z_i}\right)^{\frac{1}{8}}, \quad \frac{\Delta\theta}{T_*} = \left(10\frac{z_i}{z_0}\right)^{\frac{1}{3}}, \quad \text{for } 10^2 < \frac{z_i}{z_0} < \left(\frac{Ra}{560}\right)^{\frac{3}{8}} \tag{23}$$

in air. Here $Ra = (\beta g \Delta\theta z_i^3)/(\nu\mu)$ is the Rayleigh number in terms of $\Delta\theta$. Data reported in figure 4 of Frisch & Businger (1973) show $\Delta\theta \approx 13$ K. Unfortunately, their paper does not contain all the scales necessary to test the theoretical prediction. However, J. A. Businger (personal communication, 1988) estimates $8\text{ K} < \Delta\theta < 15\text{ K}$, $0.09\text{ K} < T_* < 0.13\text{ K}$, $750\text{ m} < z_i < 1500\text{ m}$, and $1\text{ cm} < z_0 < 2\text{ cm}$. These data define a box $60 < \Delta\theta/T_* < 170$, $4\times10^4 < z_i/z_0 < 15\times10^4$, which is crossed by the line predicted by (23). Although this supports our theory, further measurements are desirable to narrow the spread of data.

In the present study, we have performed integrations from non-dimensional time 6 to 7 with different values of the surface-roughness heights, all starting from the fields obtained for $z_i/z_0 = 10^4$ at non-dimensional time 6. We find that the flow in the surface layer adjusts up to errors below 2% to changes in the surface roughness after a time of order $0.15z_i/w_*$. Therefore, the results at non-dimensional time 7 again represent the asymptotic state.

Before we present the LES results for the surface temperature, we discuss the effect of the surface roughness on the turbulence in the CBL. Figure 21 shows profiles of the horizontal-velocity fluctuations, the vertical-velocity skewness, and the dissipation rate. Figure 21 (*a*) shows that increased roughness height causes reduced horizontal-velocity fluctuations mainly in the surface layer. This is the expected effect of increased friction over rough surfaces. However, the short dashed curve shows that the mixed layer is also affected by surface roughness if the roughness is very large ($z_0/z_i = 10^{-2}$).

The skewness profiles, figure 21*b*, indicate high sensitivity to surface roughness. Note that the expression $-\partial\langle w^3\rangle/\partial z$ forms a source term in the budget equation of vertical-velocity variance. At the surface, w^3 is zero. Thus, the source term in the lowest grid cell is negative if $\langle w^3\rangle > 0$ at the top of the first grid cell. If the skewness changes from positive to negative values, this source term changes from negative to positive in the lowest layer of the computation. Thus negative skewness implies that kinetic energy is transported down into the lowest grid cell by turbulent transport whereas the expected positive value implies the opposite.

Our model predicts negative skewness near the surface for large roughness heights but large positive skewness values for small roughness heights. This strong dependence is presumably unrealistic and an effect of deficiencies in the SGS model near the surface. As already noted above in discussing figures 7 and 8, small changes in the coefficient c_l, which affects the dissipation rate in the lowest grid cell, may change the sign of the skewness. Figure 21(*c*) shows that the dissipation rate increases near the surface if z_0 is increased relative to the reference value. However, at somewhat higher z-levels, the dissipation rate also increases for reduced roughness height, presumably owing to increased velocity fluctuations at these intermediate levels. At the surface itself, we expect from neutral Prandtl-layer theory that the dissipation rate varies as $\langle\epsilon\rangle = u_*^3/(\kappa z)$, where $\kappa = 0.41$ is the von Kármán constant. For the case of zero mean wind, we replace u_* by the minimum friction velocity $\tilde{u}_*$ and obtain from (23)

$$\langle\epsilon\rangle = 0.34\frac{w_*^3}{z}\left(\frac{z_0}{z_i}\right)^{\frac{1}{3}}. \tag{24}$$

This equation underestimates the dissipation rate except for heights that are small in comparison with the effective Obukhov length where buoyancy forces are negligible in comparison with fluctuating shear forces. At the lowest grid level, at $z/z_i = 1/64$, it predicts the values $\langle\epsilon\rangle z_i/w_*^3 = (0.022, 0.22, 2.2)$ for $z_0/z_i = (10^{-6}, 10^{-4}, 10^{-2})$, respectively. For $z_0/z_i \leqslant 10^{-4}$ the values show that the shear contribution to the surface dissipation rate is negligible. But for $z_0/z_i = 10^{-2}$, equation (24) does predict the increased dissipation rate, which even exceeds the buoyancy forcing at the surface.

These findings suggest the following explanation for negative skewness at low levels in the LES. Large roughness heights induce excessive dissipation rates which cause an energy imbalance that drives downward transport of kinetic energy by turbulent 'diffusion' for equilibrium. For small values of z_0/z_i, on the other hand, the kinetic energy produced at low levels exceeds the dissipation rate and therefore positive skewness arises which indicates upwards energy transport. Thus, large positive (negative) skewnesses near the surface are the consequence of too small (too large) surface dissipation rates relative to the buoyancy production rate.

In view of this explanation it is no longer surprising that Willis & Deardorff (1974) find negative triple correlations near the bottom of their water tank. In this experiment the effective Reynolds number is not large and viscous dissipation at the surface causes an imbalance which drives downward turbulent transport. As an interesting analogy we point out that negative triple moments of the normal velocity fluctuations are also found in the viscous layer of a pure shear boundary-layer in direct numerical simulations by Spalart (1988). As a consequence he finds that turbulent diffusion provides a source of velocity variance in the viscous layer, whereas it represents a sink in the fully turbulent part of the boundary layer (see figure 24*b* in Spalart 1988). In the present LES, excessive SGS damping has the same effect as viscosity in the viscous layer. Our explanation is also consistent with the

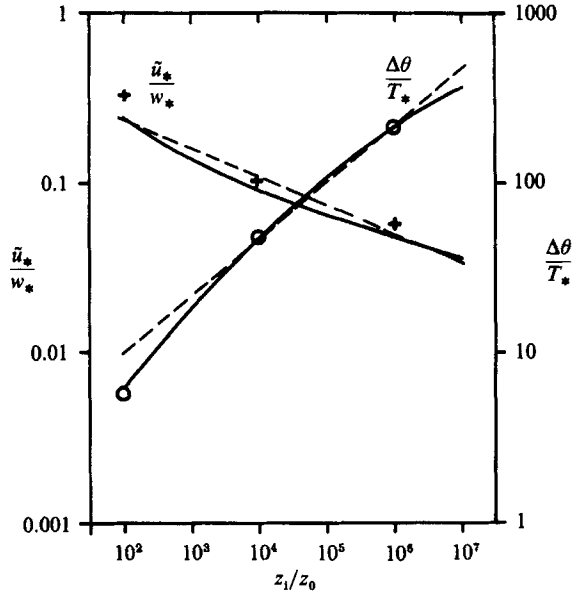

FIGURE 22. Minimum friction velocity $\tilde{u}_*$ over the convective velocity scale w_* and temperature difference $\Delta\theta$ over the convective temperature scale T_* versus the boundary layer/roughness height ratio z_1/z_0: ——, prediction of Schumann's (1988) model; ---- approximations given by (23); + (○), LES results ($t_* = 7$) for the friction velocity (temperature difference).

result of Mason (1987) who found that the skewness is negative for small SGS diffusivities but becomes positive for large values of the SGS diffusivity. This diffusivity determines the dissipation rate in the mixed layer for more or less constant surface friction. Moreover, the explanation given is consistent with the effect of c_l on the skewness as found in figure 8.

Hence, the correct (positive) skewness is obtained only if a delicate balance is achieved between the SGS model for the mixed layer, the SGS model for the lowest grid-cell layer and the model for the momentum fluxes at the surface. However, the general results presented in this paper show that deficiencies in this respect do not cause the results for the bulk of the CBL to deteriorate.

We now turn to figure 22 in which we have plotted the prediction of Schumann (1988) (full curves) and his approximation reported in equation (23) (dashed lines). The symbols for three values of the surface roughness represent the results of the LES. We find that the LES results agree very well with the predictions and do support the model's results. In particular, the LES results corroborate the curved trend shown by the full curves in figure 22. For the reference case, we obtain $z_1/z_0 = 1.065 \times 10^4$, $\tilde{u}_*/w_* = 0.1077$, $\Delta\theta/T_* = 49.01$. From the case with reduced SGS diffusivities for the same roughness height (for which results are shown in figures 11 and 15*b*) we obtain $\tilde{u}_*/w_* = 0.1096$, $\Delta\theta/T_* = 48.97$. The differences amount to less than 2% and thus show the weak dependence of these results on model parameters.

4. Summary and discussion

We have presented results of a large-eddy simulation of the convective boundary layer obtained with quite fine resolution. The LES method uses a second-order closure subgrid-scale model. In the present application this feature is of minor

importance because of the fine resolution, except for the inversion layer where simple models tend to produce excessive negative SGS heat flux. In future applications one should reduce the coefficient c_{BT} in (8) to ensure small but positive SGS heat fluxes in the interfacial layer. The boundary condition at the surface applies the Monin–Obukhov-relationships. These relationships require stationary flow, which is not satisfied for the instantaneous fields and thus might be a source of errors which cannot be quantified from this study. However, the flow near the surface is approximately stationary both with respect to ensemble and conditional mean values. Most sensitive to details of the models are the inertia-range spectra in the interior of the flow, the skewness of the vertical velocity near the surface and the decay of gravity waves above the inversion. Our model gives approximately correct spectra with a set of model coefficients that is derived from the well-established inertia-range spectra without empirical adjustment. We have performed further simulations with coarser grids (Schmidt 1988) which support these findings. The mean profiles generally also agree very well with Deardorff's (1974) LES results which he obtained with much lower resolution (40^3 grid cells in a domain of 5 km × 5 km × 2 km) and even slightly smaller SGS-diffusivities (compare table 1). This agreement, our well-behaved spectra and the small sensitivity to changes in the SGS coefficients show that our results do not suffer strongly from large finite-difference errors. The correct skewness is more difficult to achieve. Obviously, surface friction requires careful adjustment of the dissipation model parameters. Our experience in varying the parameter c_l, see equation (C 6), suggests that it should be slightly increased in future applications. The top boundary condition, which is as proposed by Bougeault (1983) and Klemp & Durran (1983), has been found to be successful in avoiding spurious reflections of gravity waves.

The results are in fair agreement with previous measurements and simulations as far as mean profiles and spectra of turbulence are concerned. With respect to horizontal-velocity fluctuations we have reasons to trust the results from our model and the measurements of Willis & Deardorff (1974) more than the later measurements of Deardorff & Willis (1985). Previous measurements in the atmosphere obviously overestimate the dissipation rate for zero mean wind. Also, the temperature variance seems to be smaller than commonly reported from measurements in the mixed layer. Our pressure fluctuations are smaller than those of Moeng & Wyngaard (1986) which seem to be infected by large hydrostatic oscillations in the stable layer above the CBL.

Plots of velocity and temperature fields in vertical and horizontal cross-sections illustrate the instantaneous structure of the turbulent field. Correlation functions reflect large-scale and quasi-steady coherent structures which extend over the whole CBL from the surface up to the inversion and laterally over a diameter of about $2z_i$. The autocorrelation values agree with measurements of Deardorff & Willis (1985), Hunt (1984) and Hunt *et al.* (1988). The average structure of updraughts and downdraughts has been obtained by conditional sampling. The sampling method introduced in this paper is only weakly sensitive to the sampling criterion. Owing to differences in the sampling definition, we cannot make direct comparisons with previous results obtained by conditional averaging. Amplitudes of the updraughts and downdraughts are generally larger than those published before. Both updraughts and downdraughts extend vertically over the whole CBL. The results show clearly that updraughts are composed of large-scale quasi-steady plumes together with transient rising thermals of smaller scale. This resolves earlier controversial discussions. By analysis of time derivatives, we determined the entrainment rate by

which thermals become diluted in the mixed layer. Temperature is mixed more quickly than vertical velocity. Updraughts and downdraughts are strongly correlated with quasi-steady horizontal motions near the surface and near the inversion. The pressure field differs considerably from a hydrostatic state both in shape and amplitude. Obviously, large fractions of the buoyancy forces are balanced by inertia forces due to large time derivatives rather than by pressure. For moderately small roughness heights, the convective circulation loses little momentum to the surface. Internal momentum fluxes are considerably larger.

The influence of surface roughness on the CBL has been investigated by means of a parameter study. The surface roughness, at least for $z_0/z_i > 10^{-4}$, and also the stability of the layer above the CBL, seem to be more important than generally suggested by the apparent success of the convective scaling introduced by Deardorff (1970). It may be conjectured that some of the scatter shown by experimental data in convective scales may be eliminated if these additional parameters were taken into account.

The results generally support the model proposed by Schumann (1988) except for his assumption concerning a hydrostatic-pressure approximation. The actual pressure field still drives the air in the surface layer horizontally towards the centre of updraughts but it is less important than assumed in his model. As explained, the smaller pressure gradient is balanced by smaller momentum fluxes so that the model's concept is still successful. In fact, the LES results support the final results of the simple model to a surprisingly high degree as far as the minimum friction velocity and heat transfer at the rough surface is concerned. Equation (24) gives an estimate of the dissipation rate for very small heights above the rough surface of a CBL for zero mean wind.

In summary, the coherent structure of convection in the CBL can be described as follows. Large thermals have the highest terminal velocity. They suck smaller thermals from their neighbourhood into their wake which then combine to form quasi-steady plumes. The large updraughts extend vertically over the whole CBL and have distinct boundaries. The rather narrow updraughts are surrounded by large areas of downdraughts which form for continuity. Near the surface, polygonal spoke patterns seem to be realistic features of high-Rayleigh-number convection. The pattern is that of open cells with a sinking motion at the cell centre. The polygonal pattern is induced by wide downdraughts which suppress upward motions over most of the surface and drive the surface flow radially away from the centre of downdraughts. The fluid then converges towards lines and it appears quite natural that these lines form polygonals due to competing downdraughts. Fluid heated at the surface flows, on average, towards the spikes, then along the spikes towards the hubs of the spoke pattern and then upwards. Small-scale plumes remote from the main updraughts do not merge together but die out while rising against downdraughts. From the hubs of the spokes, warm air rises within updraughts in an unsteady bubble-like manner. The cross-section of the updraughts is seldom round but, rather, highly convoluted with strong lateral entrainment. Large thermals formed within the updraughts penetrate into the stable layer and cause large-scale downward movements of wisps of extruded warm fluid. Both the large upward-penetrating thermals and the downward-moving wisps contribute to the entrainment heat flux. In the stable layer, high-amplitude large-scale temperature fluctuations, for which the thermal dissipation rate is small, accumulate from bouncing excitation by updraughts. Small upward heat flux contributes to the conversion of the potential

energy connected with these temperature fluctuations into kinetic energy and subsequent mechanical dissipation. Although details of the flow state are highly transient and thermals form and rise like bubbles non-stationarily, the plumes are organized in large-scale 'quasi-steady' patterns with timescales exceeding z_i/w_*.

Busse (1978) gives a comprehensive review of thermal convection. For laminar Rayleigh–Bénard convection, in the intermediate neighbourhood above the critical Rayleigh number, open cells or 'g-hexagons' with downward motion in the centre of the hexagons form if the viscosity increases with temperature, as is the case in gases. 'Optimum theories' explain this tendency by minimizing the mechanical dissipation rate for a given heat flux. In our case, the flow is turbulent and molecular viscosity unimportant. However, we found that downdraughts are dissipating much less than updraughts and the dissipation rate takes its maximum near the surface. Hence, open cells with wide downdraughts are dissipating less than closed cells. This is consistent with the spirit of the optimum theory. As a further mechanism for the formation of hexagonal cells, Krishnamurti (1975) has shown that open cells are selected by laminar Rayleigh–Bénard convection if the mean flow contains sinking motion. In our case, the mean flow is zero but, on scales of order z_i, sinking motion prevails and this is consistent with the formation of open cells. Still, such arguments are heuristic and have to be viewed with reservation.

The spoke pattern has also been found by Mason (1987) but it was not clear whether his results are relevant for the quasi-infinite Rayleigh numbers of the atmospheric CBL because of rather large SGS diffusivities. The present results seem to be more relevant for atmospheric cases because of the finer resolution and the smaller diffusivity. The spoke pattern has not been noted in the LES of Deardorff (1974), presumably because his plots show only cross-sections at $z/z_i = 0.4$. Figure 22 of Deardorff (1972), for $z/z_i = 0.25$, exhibits a spoke pattern in the vertical velocity and the related temperature fluctuations. (Note that his plots show negative temperature deviations along the spokes because of the selected normalization parameters.) In his discussion, Deardorff (1972) does not mention the spoke pattern; rather he identifies merging plumes. Spoke patterns are known to exist in the convective part of internally heated fluid layers at Rayleigh numbers of the order 100 times the critical one, as clearly shown in direct numerical simulations by Grötzbach (1986) and related experiments cited by him. Busse (1978) reports that for Rayleigh numbers of the order 10^5–10^7, turbulent spoke-pattern convection is observed in Rayleigh–Bénard convection experiments and represents the dominant form of convection over a wide range of Prandtl numbers. The pattern at these Rayleigh numbers is, however, more coherent than in our simulations. Grötzbach (1982) also investigated the case of Rayleigh–Bénard convection between two isothermal no-slip walls at comparable Rayleigh numbers with the same numerical method. He did not see spoke patterns in his contour plots at mid-levels of the fluid layer. However, recent additional evaluations of his results in the lower quarter of the fluid layer showed that Rayleigh–Bénard convection does also display a structure which is similar to the spoke pattern (G. Grötzbach 1988, personal communication). But his spokes are not straight and appear to be distorted by downdraughts. Note that the Rayleigh–Bénard convection between two isothermal no-slip walls is symmetric in that both warm rising and cold sinking plumes or thermals are forming at the walls, while our problem is asymmetric in that only warm plumes are generated by the boundary conditions. Because of this asymmetry, the spoke pattern is not disturbed by sinking cold plumes to the same extent as in Rayleigh–Bénard convection. Also,

the internally heated fluid layer, and presumably most of the experiments to which Busse (1978) referred, show a similar asymmetry which explains the similar spoke pattern.

Unfortunately, observations on the horizontal pattern of the CBL at high Rayleigh numbers, $Ra > 10^9$, are rare. Obviously one needs simultaneous measurements at several positions in a horizontal plane to detect this pattern. The most convincing evidence on the existence of spoke-pattern convection in the CBL stems from the laboratory investigations of Willis & Deardorff (1979). The experiment was performed in a water tank filled initially with stably stratified fluid and heated from below. Motions were made visible by introducing milk into the lowest level of the water layer. The Rayleigh number of these experiments was about 10^9 and the turbulent Reynolds number associated with the dominant motions in the tank was 1200. Photographs of the convective pattern as reported by Willis & Deardorff (1979) indicate very close similarity between these experiments and our numerical simulations. Radar observations of Konrad (1970) obviously identify the upper parts of the mixed layer with plumes penetrating into the stable layer and causing the rings of warm air which we see at $z/z_i = 1$ in figure 14(v). The dual Doppler-radar observations of Frisch *et al.* (1976) display the flow pattern for one instant of time; they clearly show convergence lines at a height of 100 m separated by about 4.5 km. The depth of the boundary layer is not reported in that paper but can be estimated to amount at least to 1.2 km. Grossman (1982) reports on spectra of vertical-velocity fluctuations measured on board an aircraft flying over sea at low flight levels (18 m). He claims that he observed two significant peaks of energy, one at a wavelength of the order of a few hundred metres and a second at a wavelength of a few kilometres in an approximately 600 m deep CBL. Based on these observations he postulates that the CBL shows a random pattern of vortex rings at small wind speeds. He does not discuss the possibility of a spoke pattern but his observations also corroborate this pattern. Woodcock & Wyman (1947) observed the lateral displacement of smoke released from stationary sources at sea and show that these displacements are consistent with a convective pattern of hexagonal cells. However, Ludlam & Scorer (1953) classify this evidence as suggestive rather than compelling. Lyons & Pease (1972) observe 'steam devils' in cold air flowing over a lake. They show photographs that suggest that there were quasi-hexagonal cells elongated along the surface wind direction. The largest steam devils of 50–200 m in diameter rose from the vertices of the hexagons to a height of 500 m. Hess *et al.* (1988) report further observations of such vortices and show that they occur for $-z_i/L > 50$ (L = Obukhov length). As summarized by Wilczak & Tillman (1980), Webb (1984) and Hess *et al.* (1988), Webb (1977) determined surface wind flow patterns with an array of seven wind vanes, placed at 100 m intervals across the mean wind direction. For unstable conditions with light winds, strong convergence lines, 50–100 m thick, were found. These lines are sometimes arranged in an irregular polygonal pattern. The spacing between each convergence line amounts to several kilometres. The convergent surface flow exhibits largest velocities near and towards the knots of the polygonal lines. Wilczak & Tillman (1980) have also used an array of sensors to observe the spatial structure of plumes at small heights. The separation of their sensors was too small (7 along a line of 100 m distance) to identify the large-scale structure. However, in light wind they observe meandering lines of isotherms which may be caused by the same pattern as observed by Webb. Hence, evidence is accumulating which suggests that the spoke pattern is a realistic feature of the lower half of the atmospheric CBL.

The spoke pattern is connected with temperature fluctuations of the order $10T_*$

which amounts typically to 1 K for atmospheric cases. The amplitude of temperature fluctuations due to surface inhomogeneities very likely exceeds this level of temperature variance. Hence, we expect that the spoke pattern is easily destroyed over inhomogeneous surfaces. We have found little sensitivity of the spoke pattern to small-scale disturbances in terms of the SGS model. But it appears likely that the sensitivity will be large at scales of order z_i. For this reason and because of the large-scale measurements required, it is not surprising that the spoke pattern is not observed more often in field observations.

Appendix A. Explicit form of the second-order-closure subgrid-scale equations

The SOC-SGS model, equations (7)–(9), can be rewritten as

$$\overline{A''_{ij}} = -\frac{l}{c_{Rm}\overline{E''}^{\frac{1}{2}}}\left[(1-c_{Gm})\tfrac{2}{3}\overline{E''}\left(\frac{\partial\bar{u}_i}{\partial x_j}+\frac{\partial\bar{u}_j}{\partial x_i}\right)+\overline{B''_{ij}}\right], \tag{A 1}$$

$$\overline{B''_{ij}} = (1-c_{Bm})\beta g(\overline{u''_j T''}\delta_{i3}+\overline{u''_i T''}\delta_{j3}-\tfrac{2}{3}\delta_{ij}\overline{u''_3 T''}), \tag{A 2}$$

$$\overline{u''_i T''} = -\frac{l}{c_{RT}\overline{E''}^{\frac{1}{2}}}\left[(1-c_{GT})\tfrac{2}{3}\overline{E''}\frac{\partial\bar{T}}{\partial x_i}-(1-c_{BT})\beta g\overline{T''^2}\delta_{i3}\right], \tag{A 3}$$

$$\overline{T''^2} = -\frac{2l}{c_{\epsilon T}\overline{E''}^{\frac{1}{2}}}\left[\overline{u''_i T''}\frac{\partial\bar{T}}{\partial x_i}\right]. \tag{A 4}$$

In this form, it becomes obvious that the buoyancy fluxes cause a deviation from the pure gradient-flux form.

The above equations form a linear system for the fluxes and the temperature variance. It can be solved explicitly. Using the abbreviations

$$c_\nu = \frac{2}{3}\frac{1-c_{Gm}}{c_{Rm}}, \quad c_B = \frac{4}{9}\frac{(1-c_{Bm})(1-c_{GT})}{c_{Rm}c_{RT}}, \tag{A 5}$$

and

$$c_\gamma = \frac{2}{3}\frac{1-c_{GT}}{c_{RT}}, \quad G = \frac{2(1-c_{BT})}{c_{RT}c_{\epsilon T}}\frac{\beta g l^2}{\overline{E''}}, \tag{A 6}$$

we obtain

$$\overline{A''_{11}} = -c_\nu l\overline{E''}^{\frac{1}{2}}2\frac{\partial\bar{u}}{\partial x}-c_B l^2\beta g\left\{\frac{\partial\bar{T}}{\partial z}-\frac{G}{1+G\,\partial\bar{T}/\partial z}\left(\frac{\partial\bar{T}}{\partial x_i}\right)^2\right\}, \tag{A 7}$$

$$\overline{A''_{22}} = -c_\nu l\overline{E''}^{\frac{1}{2}}2\frac{\partial\bar{v}}{\partial y}-c_B l^2\beta g\left\{\frac{\partial\bar{T}}{\partial z}-\frac{G}{1+G\,\partial\bar{T}/\partial z}\left(\frac{\partial\bar{T}}{\partial x_i}\right)^2\right\}, \tag{A 8}$$

$$\overline{A''_{33}} = -c_\nu l\overline{E''}^{\frac{1}{2}}2\frac{\partial\bar{w}}{\partial z}+2c_B l^2\beta g\left\{\frac{\partial\bar{T}}{\partial z}-\frac{G}{1+G\partial\bar{T}/\partial z_i}\left(\frac{\partial\bar{T}}{\partial x_i}\right)^2\right\}, \tag{A 9}$$

$$\overline{w''T''} = -c_\gamma l\overline{E''}^{\frac{1}{2}}\left[\frac{\partial\bar{T}}{\partial z}-\frac{G}{1+G\,\partial\bar{T}/\partial z}\left(\frac{\partial\bar{T}}{\partial x_i}\right)^2\right], \tag{A 10}$$

$$\overline{T''^2} = 2\frac{c_\gamma}{c_{\epsilon T}}\frac{l^2}{1+G\,\partial\bar{T}/\partial z}\left(\frac{\partial\bar{T}}{\partial x_i}\right)^2. \tag{A 11}$$

Once these fluxes are computed, the remaining flux components follow from (A 1)–(A 3). The temperature variance is needed explicitly for diagnostic purposes only.

In order to ensure finite positive solutions, we replace the expression $\{1 + G\partial\bar{T}/\partial z\}$ by unity if it becomes less than one. This approach has also been used by Schemm & Lipps (1976). The fluxes are computed on a staggered grid to minimize spatial averaging.

Appendix B. Determination of the SGS-model coefficients

As shown by Lilly (1967), all essential SGS-model coefficients can be determined by application of inertial–convective subrange theory of isotropic turbulence (e.g. see Hinze 1959). However, a consistent description of the theory for determination of the coefficients in the SOC-model is missing. Moreover, the following analysis enables us to compare our model with previous proposals. The theory assumes non-buoyant turbulence. This is a reasonable restriction because of the small correlation between vertical-velocity fluctuations and temperature fluctuations at small scales, i.e. for locally isotropic turbulence.

In the inertial–convective subrange of isotropic turbulence, the spectra of kinetic energy $\langle u_i'^2/2\rangle$ and temperature variance $\langle T'^2\rangle$ integrated over all wavenumbers of magnitude k follow the well-known relationships

$$E(k) = \alpha\langle\epsilon\rangle^{\frac{2}{3}}k^{-\frac{5}{3}}, \quad E_T(k) = \beta\langle\epsilon_T\rangle\langle\epsilon\rangle^{-\frac{1}{3}}k^{-\frac{5}{3}}, \tag{B 1}$$

where the dissipation rates of kinetic energy and one half the temperature variance are

$$\langle\epsilon\rangle = \frac{1}{2}\left\langle\nu\left(\frac{\partial u_i}{\partial x_j}+\frac{\partial u_j}{\partial x_i}\right)^2\right\rangle, \quad \langle\epsilon_T\rangle = \left\langle\mu\left(\frac{\partial T}{\partial x_j}\right)^2\right\rangle. \tag{B 2}$$

The coefficients α and β of the 'three-dimensional' spectra are related to the coefficients α_1 and β_1 of one-dimensional longitudinal velocity and temperature spectra according to Hinze (1959), equations (3–72, 3–187), by

$$\alpha = \tfrac{55}{18}\alpha_1, \quad \beta = \tfrac{5}{3}\beta_1. \tag{B 3}$$

These 'one-dimensional' coefficients have been measured many times. A recent summary of knowledge and new data are given by Andreas (1987). These measurements imply

$$\alpha = 1.6 \pm 0.02, \quad \beta = 1.34 \pm 0.02. \tag{B 4}$$

As Lilly (1967), we assume that the cut-off wavenumber which separates the resolved from the SGS motions is π/Δ, where Δ is the characteristic grid spacing. We know that this assumption is a crude approximation in principle, where finite-difference approximations are being used, and more accurate approaches are known, see Schumann (1975). However, the extra effort does not pay off in view of the insensitivity of results (Grötzbach & Schumann 1979). Moreover, we assume that the contributions of the resolved scales to the deformation tensor can still be approximated by the inertial-range theory although the actual spectrum must deviate from the $k^{-\frac{5}{3}}$ form in the range of resolved wavenumbers. Again, experience suggests that this approximation gives reasonable results. Of course, this is because this part of the spectrum is weighted with a factor k^2 before integration, see (B 7) and (B 8) below. Thus we use the spectra to determine

$$\langle\overline{E''}\rangle = \int_{\pi/\Delta}^{\infty} E(k)\,\mathrm{d}k = \frac{3\alpha}{2}\langle\epsilon\rangle^{\frac{2}{3}}\left(\frac{\Delta}{\pi}\right)^{\frac{2}{3}}, \tag{B 5}$$

$$\langle \overline{T''^2} \rangle = \int_{\pi/\Delta}^{\infty} E_T(k)\,\mathrm{d}k = \frac{3\beta}{2}\langle \epsilon_T \rangle \langle \epsilon \rangle^{-\frac{1}{3}} \left(\frac{\Delta}{\pi}\right)^{\frac{2}{3}}, \tag{B 6}$$

$$\langle D \rangle = \frac{1}{2}\left\langle \left(\frac{\partial \bar{u}_i}{\partial x_j} + \frac{\partial \bar{u}_j}{\partial x_i}\right)^2 \right\rangle = 2\int_0^{\pi/\Delta} k^2 E(k)\,\mathrm{d}k = \frac{3\alpha}{2}\langle \epsilon \rangle^{\frac{2}{3}} \left(\frac{\pi}{\Delta}\right)^{\frac{4}{3}}, \tag{B 7}$$

$$\langle D_T \rangle = \left\langle \left(\frac{\partial \bar{T}}{\partial x_j}\right)^2 \right\rangle = \int_0^{\pi/\Delta} k^2 E_T(k)\,\mathrm{d}k = \frac{3\beta}{4}\langle \epsilon_T \rangle \langle \epsilon \rangle^{-\frac{1}{3}} \left(\frac{\pi}{\Delta}\right)^{\frac{4}{3}}. \tag{B 8}$$

Comparing these results with the closure assumptions

$$\epsilon = c_{\epsilon m} \frac{\overline{E''}^{\frac{3}{2}}}{\Delta}, \quad 2\epsilon_T = c_{\epsilon T} \frac{\overline{E''}^{\frac{1}{2}}}{\Delta} \overline{T''^2}, \tag{B 9}$$

and using the approximations

$$\langle \overline{E''}^{\frac{3}{2}} \rangle \approx \langle \overline{E''} \rangle^{\frac{3}{2}}, \quad \langle \overline{E''}^{\frac{1}{2}} \overline{T''^2} \rangle \approx \langle \overline{E''} \rangle^{\frac{1}{2}} \langle \overline{T''^2} \rangle, \tag{B 10}$$

gives

$$c_{\epsilon m} = \left(\frac{2}{3\alpha}\right)^{\frac{3}{2}} \pi, \quad c_{\epsilon T} = \frac{4}{3\beta}\left(\frac{2}{3\alpha}\right)^{\frac{1}{2}} \pi. \tag{B 11}$$

A gradient model

$$\overline{u_i'' u_j''} = -\nu_t \left(\frac{\partial \bar{u}_i}{\partial x_j} + \frac{\partial \bar{u}_j}{\partial x_i}\right) + \tfrac{1}{3}\delta_{ij} \overline{u''^2_k}, \quad \overline{u_i'' T''} = -\gamma_t \frac{\partial \bar{T}}{\partial x_i} \tag{B 12}$$

with the Prandtl–Kolmogorov diffusivities

$$\nu_t = c_\nu \Delta \overline{E''}^{\frac{1}{2}}, \quad \gamma_t = c_\gamma \Delta \overline{E''}^{\frac{1}{2}} \tag{B 13}$$

causes energy and temperature-variance production rates

$$\langle P \rangle = \left\langle -\overline{u_i'' u_j''} \frac{\partial \bar{u}_i}{\partial x_j} \right\rangle = c_\nu \langle \Delta \overline{E''}^{\frac{1}{2}} D \rangle, \tag{B 14}$$

$$\langle P_T \rangle = \left\langle -\overline{u_i'' T''} \frac{\partial \bar{T}}{\partial x_i} \right\rangle = c_\gamma \langle \Delta \overline{E''}^{\frac{1}{2}} D_T \rangle. \tag{B 15}$$

For local equilibrium turbulence, these production rates equal the respective dissipation rates. From this condition, and approximations similar to those in (B 10), we obtain with (B 7) and (B 8):

$$c_\nu = \left(\frac{2}{3\alpha}\right)^{\frac{3}{2}} \frac{1}{\pi}, \quad c_\gamma = \left(\frac{2}{3\alpha}\right)^{\frac{1}{2}} \frac{4}{3\beta} \frac{1}{\pi}. \tag{B 16}$$

In the absence of buoyancy, the SOC model, (7)–(9), reduces to the gradient model, (B 12) and (B 13), with

$$c_\nu = \frac{2}{3} \frac{1 - c_{Gm}}{c_{Rm}}, \quad c_\gamma = \frac{2}{3} \frac{1 - c_{GT}}{c_{RT}}. \tag{B 17}$$

This shows that the various coefficients used to model the redistribution terms due to pressure fluctuations cannot be selected independently. Comparing our model with those of Schemm & Lipps (1976) and Sommeria (1976) shows that they used $c_{Gm} = \frac{3}{5}$, $c_{Bm} = c_{GT} = 0$, $c_{BT} = \frac{1}{3}$. Thus they neglect some of the redistribution terms. We follow Gibson & Launder (1976) who reviewed several theoretical and

experimental studies and recommend $c_{Gm} = c_{Bm} = 0.55$, $c_{GT} = c_{BT} = 0.50$. From all these equations, we finally obtain the numerical values as given in table 1 (see § 2.2).

The large value of the coefficient c_{Rm} suggests that SGS turbulence is very effective in reducing anisotropy. Equation (B 13) implies a turbulent Prandtl number for the SGS

$$\frac{c_\nu}{c_\gamma} = \frac{\beta}{2\alpha} = 0.42. \tag{B 18}$$

A value below unity means that temperature is mixed more effectively than momentum by small-scale turbulence. The present turbulent Prandtl number is close to the value 0.4 in the models of Deardorff (1973), Sommeria (1976), and Schemm & Lipps (1976) and only a little larger than the value 0.39 of Grötzbach & Schumann (1979).

The only coefficient which is determined by pure guesswork is c_{3m}. This coefficient controls the SGS diffusion of SGS energy. Here we follow the estimates of Deardorff (1973), and Schemm & Lipps (1976) and set $c_{3m} = 0.2$. It suggests a rather small turbulent Prandtl number for SGS kinetic energy, $(3/5)c_\nu/c_{3m} = 0.25$.

For the purpose of comparison with other models, it is helpful to identify the coefficients in the classical Smagorinsky-type eddy-diffusivity models (for negligible buoyancy)

$$\nu_t = (c_S \Delta)^2 D^{\frac{1}{2}}, \quad \gamma_t = (c_{ST} \Delta)^2 D^{\frac{1}{2}}, \tag{B 19}$$

which are related to the previous coefficients by

$$c_S = \left(\frac{c_\nu^3}{c_{\epsilon m}}\right)^{\frac{1}{4}} = \frac{1}{\pi}\left(\frac{2}{3\alpha}\right)^{\frac{3}{4}} = 0.165, \tag{B 20}$$

$$c_{ST} = c_\gamma^{\frac{1}{2}}\left(\frac{c_\nu}{c_{\epsilon m}}\right)^{\frac{1}{4}} = \frac{1}{\pi}\left(\frac{2}{3\alpha}\right)^{\frac{1}{4}}\left(\frac{4}{3\beta}\right)^{\frac{1}{2}} = 0.255. \tag{B 21}$$

The values of the various coefficients are given in table 1 where they are compared to those in other models. We see from this table that our model is in general agreement with models of Deardorff (1974, 1980), Schemm & Lipps (1976), Sommeria (1976), Moeng (1984), and Grötzbach & Schumann (1979). However, some differences are notable. Our larger value for $c_{\epsilon T}$ implies smaller SGS temperature fluctuations. Large values of the Smagorinsky coefficients imply strong damping of fine-scale resolved velocity and temperature fluctuations. Grötzbach & Schumann (1979) used the smallest Smagorinsky coefficients but for non-buoyant flows. They found little sensitivity of mean fields to these coefficients. Mason (1987) applied his model with various values of c_S and c_{ST}. In most of his applications he used rather large coefficients in the Smagorinsky-type model with strong damping of the resolved eddies. On the other hand, Mason & Thomson (1987) obtain most convincing results for the neutral planetary boundary layer with $c_S = 0.12$.

Appendix C. The effective lengthscale

The lengthscale l is set to Δ, the mean grid size, inside the domain. Near the surface, one expects that the effective lengthscale is smaller and limited by Prandtl's mixing length κz, where κ is the von Kármán constant ($\kappa = 0.41$). By comparing (B 19) with the common mixing-length model, we see that the effective limitation for the present set of model coefficients would be

$$l = \min(\Delta, \kappa z/c_S). \tag{C 1}$$

However, for cubical mesh cells, this minimum function, or related functions as used by Mason & Callen (1986) and Mason (1987), has little or no effect because it implies $l = \Delta$ everywhere, even in the lowest mesh cell where $z = \Delta/2$ because $c_S < \kappa/2$. This is different in Mason's applications because he uses vertically refined meshes near the surface.

But, there is another reason to limit the lengthscale. Note that near the surface, the SGS contribution to buoyancy is large. Thus we can assume that the shear contributions are relatively small for zero mean flow. Close to the wall, for local equilibrium between buoyancy forcing and energy dissipation, the model equations (5) and (A 9) predict

$$\frac{\langle \overline{E''} \rangle}{w_*^2} = c_{\epsilon m}^{-\frac{2}{3}} \left(\frac{l}{z_i}\right)^{\frac{2}{3}}, \tag{C 2}$$

$$\frac{\langle \overline{w''^2} \rangle}{w_*^2} = c_{\epsilon m}^{-\frac{2}{3}} \left(\frac{l}{z_i}\right)^{\frac{2}{3}} \left[\frac{2}{3} + \frac{4}{3}\frac{(1-c_{Bm})\,c_{\epsilon m}}{c_{Rm}}\right]. \tag{C 3}$$

From measurements of Kaimal *et al.* (1976), we know that the total vertical velocity variance near the surface closely follows the relationship

$$\frac{\langle w'^2 \rangle}{w_*^2} = 1.8 \left(\frac{z}{z_i}\right)^{\frac{2}{3}}. \tag{C 4}$$

The SGS velocity variance should stay less than this result. This requires a limitation of l:

$$l < \frac{1.8^{\frac{3}{2}} c_{\epsilon m}}{\left[\frac{2}{3} + \frac{4}{3}\frac{(1-c_{Bm})\,c_{\epsilon m}}{c_{Rm}}\right]^{\frac{3}{2}}} z \approx 3.3 c_{\epsilon m}\, z. \tag{C 5}$$

In fact, the SGS variance should stay considerably below the total variance. Therefore, we use

$$l = \min(\Delta, c_l z). \tag{C 6}$$

Equation (C 5) shows that this limitation should depend mainly on the SGS coefficient for dissipation, $c_{\epsilon m}$. The final value of c_l has, however, to be determined empirically. Our preliminary simulations lead us to suggest $c_l = c_{\epsilon m}$ in most cases unless stated otherwise.

Alternatively, we could have followed Deardorff (1980) and Moeng (1984) who increased $c_{\epsilon m}$ in the lowest grid cell by a 'wall-effect' factor of up to 3.9 to prevent $\overline{E''}$ from becoming unduly large there. Such an increase of $c_{\epsilon m}$ would have the same effect as a reduction of l, but the present approach offers at least some formal guidance for this procedure.

Appendix D. Monin–Obukhov boundary conditions

The Monin–Obukhov relationships are used to determine the friction velocity u_*, i.e. the square root of the kinematic surface stress, for given horizontal velocity in the first interior mesh cell. One should be aware of the limitations of these relationships (homogeneity and stationarity of the surface layer) but no better simple alternative is known and the effects of surface friction are relatively small for the mixed layer. The actual relationships are as proposed by Paulson (1970) and Dyer (1974):

$$U(z) = \frac{u_*}{\kappa}\left[\ln\left(z/z_0\right) - \psi_m\left(\frac{z}{L}\right) + \psi_m\left(\frac{z_0}{L}\right)\right], \tag{D 1}$$

$$T(z)-\theta_s = \frac{\theta_*}{\kappa}\left[\ln\left(\frac{z}{z_0}\right)-\psi_h\left(\frac{z}{L}\right)+\psi_h\left(\frac{z_0}{L}\right)\right], \tag{D 2}$$

$$\theta_* = -\frac{Q_s}{u_*}, \quad L = -\frac{u_*^3}{\kappa\beta g Q_s}, \tag{D 3}$$

$$\psi_m(\zeta) = 2\ln\left(\frac{1+\phi_m^{-1}}{2}\right)+\ln\left(\frac{1+\phi_m^{-2}}{2}\right)-2\arctan(\phi_m^{-1})+\frac{\pi}{2}, \tag{D 4}$$

$$\psi_h(\zeta) = 2\ln\left(\frac{1+\phi_h^{-1}}{2}\right), \tag{D 5}$$

$$\phi_m(\zeta) = (1-16\zeta)^{-\frac{1}{4}}, \quad \phi_h(\zeta) = (1-16\zeta)^{-\frac{1}{2}}, \quad \kappa = 0.41. \tag{D 6}$$

These equations apply to the unstable case, i.e. for $z/L \leqslant 0$, where the Obukhov length L is negative. For given velocity magnitude $U(z) = (\bar{u}_1^2+\bar{u}_2^2)^{\frac{1}{2}}(z)$ in the first grid cell at $z = \Delta z/2$, we determine u_*, the friction velocity, by inverting (D 1) together with (D 3) and (D 4). Actually, by adding the small convective velocity $0.07(\beta g Q_s \Delta z)^{\frac{1}{3}}$, connected with the grid size, we increase $U(z)$ to avoid singular solutions for zero flow velocities. A Newton iteration inverts the equations to sufficient accuracy within three iterations. Then the surface stresses are given by

$$\overline{u_i'' w''} = -\frac{\bar{u}_i(z)}{U(z)}u_*^2, \quad i = 1, 2. \tag{D 7}$$

The surface temperature $\theta_s \equiv T(z_0)$ is required for diagnostic purposes only, and computed from (D 2) for a given temperature $T(z)$ at the level $z = \Delta z/2$. Gradients of horizontal velocity and temperature at the surface have to be known in order to compute the shear production rate of kinetic energy and gradient production rate of temperature variance from products of fluxes and gradients. They are computed from

$$\frac{\partial \bar{u}_i}{\partial z} = \frac{\bar{u}_i(z)}{U(z)}\frac{u_*}{\kappa\Delta z/2}, \quad \frac{\partial \bar{T}}{\partial z} = \frac{\theta_*}{\kappa\Delta z/2}, \tag{D 8}$$

where Δz is the vertical mesh spacing.

REFERENCES

Adrian, R. J., Ferreira, R. T. D. S. & Boberg, T. 1986 Turbulent thermal convection in wide horizontal fluid layers. *Exps Fluids* **4**, 121–141.

André, J. C., De Moor, G., Lacarrerre, P., Therry, G. & du Vachat, R. 1978 Modeling the 24-hour evolution of the mean and turbulent structures of the planetary boundary layer. *J. Atmos. Sci.* **35**, 1861–1883.

Andreas, E. L. 1987 Spectral measurements in a disturbed boundary layer over snow. *J. Atmos. Sci.* **44**, 1912–1939.

Bougeault, P. 1983 A non-reflective upper boundary condition for limited-height hydrostatic models. *Mon. Wea. Rev.* **111**, 420–429.

Businger, J. A. 1973 A note on free convection. *Boundary-Layer Met.* **4**, 323–326.

Busse, F. H. 1978 Non-linear properties of thermal convection. *Rep. Prog. Phys.* **41**, 1930–1967.

Busse, F. H. & Whitehead, J. A. 1974 Oscillatory and collective instabilities in large Prandtl number convection. *J. Fluid Mech.* **66**, 67–79.

Carruthers, D. J. & Moeng, C.-H. 1987 Waves in the overlying inversion of the convective boundary layer. *J. Atmos. Sci.* **44**, 1801–1808.

CAUGHEY, S. J. 1982 Observed characteristics of the atmospheric boundary layer. In *Atmospheric Turbulence and Air Pollution Modelling* (ed. F. T. M. Nieuwstadt & H. van Dop), pp. 107–158. Reidel.

CAUGHEY, S. J. & PALMER, S. G. 1979 Some aspects of turbulence structure through the depth of the convective boundary layer. *Q. J. R. Met. Soc.* **105**, 811–827.

CHATFIELD, R. B. & BROST, R. A. 1987 A two-stream model of the vertical transport of trace species in the convective boundary layer. *J. Geophys. Res.* **92**, D11, 13263–13276.

CHEN, C. & COTTON, W. R. 1983 Numerical experiments with a one-dimensional higher order turbulence model: Simulation of the Wangara day 33 case. *Boundary-Layer Met.* **25**, 374–404.

COULMAN, C. E. 1970 Fluctuations of horizontal wind speed near the ground in convective conditions. *Q. J. R. Met. Soc.* **96**, 529–534.

CRUM, T. D., STULL, R. B. & ELORANTA, E. W. 1987 Coincident Lidar and aircraft observations of entrainment into thermals and mixed layers. *J. Clim. Appl. Met.* **26**, 774–778.

DEARDORFF, J. W. 1970 Convective velocity and temperature scales for the unstable planetary boundary layer and for Rayleigh convection. *J. Atmos. Sci.* **27**, 1211–1213.

DEARDORFF, J. W. 1971 On the magnitude of the subgrid scale eddy coefficient. *J. Comput. Phys.* **7**, 120–133.

DEARDORFF, J. W. 1972 Numerical investigation of neutral and unstable planetary boundary layers. *J. Atmos. Sci.* **29**, 91–115.

DEARDORFF, J. W. 1973 The use of subgrid transport equations in a three-dimensional model of atmospheric turbulence. *Trans. ASME* I: *J. Fluids Engng* **95**, 429–438.

DEARDORFF, J. W. 1974 Three-dimensional numerical study of turbulence in an entraining mixed layer. *Boundary-Layer Met.* **7**, 199–226.

DEARDORFF, J. W. 1980 Stratocumulus-capped mixed layers derived from a three-dimensional model. *Boundary-Layer Met.* **18**, 495–527.

DEARDORFF, J. W. & WILLIS, G. E. 1985 Further results from a laboratory model of the convective planetary boundary layer. *Boundary-Layer Met.* **32**, 205–236.

DRUILHET, A., FRANGI, J. P., GUEDALIA, D. & FONTAN, J. 1983 Experimental studies of the turbulence structure parameters of the convective boundary layer. *J. Clim. Appl. Met.* **22**, 594–608.

DYER, A. J. 1974 A review of flux-profile relationships. *Boundary-Layer Met.* **7**, 363–372.

FINGER, J. E. & SCHMIDT, H. 1986 On the efficiency of higher order turbulence models simulating the convective boundary layer. *Beitr. Phys. Atm.* **59**, 505–517.

FRISCH, A. S. & BUSINGER, J. A. 1973 A study of convective elements in the atmospheric surface layer. *Boundary-Layer Met.* **3**, 301–328.

FRISCH, A. S., CHADWICK, R. B., MONINGER, W. R. & YOUNG, J. M. 1976 Observations of boundary-layer convection cells measured by dual-doppler radar and echosonde, and by microbarograph array. *Boundary-Layer Met.* **10**, 55–68.

GAL-CHEN, T. & KROPFLI, R. A. 1984 Buoyancy and pressure perturbations derived from dual-doppler radar observations of the planetary boundary layer: Applications for matching models with observations. *J. Atmos. Sci.* **41**, 3007–3020.

GERZ, T., SCHUMANN, U. & ELGHOBASHI, S. E. 1989 Direct numerical simulation of stratified homogeneous turbulent shear flows. *J. Fluid Mech.* **200**, 563–594.

GIBSON, M. M. & LAUNDER, B. E. 1976 On the calculation of horizontal, turbulent, free shear flows under gravitational influence. *Trans. ASME* C: *J. Heat Transfer* **98**, 81–87.

GROSSMAN, R. L. 1982 An analysis of vertical velocity spectra obtained in the BOMEX fair-weather, trade-wind boundary layer. *Boundary-Layer Met.* **23**, 323–357.

GROSSMAN, R. L. 1984 Bivariate conditional sampling of moisture flux over a tropical ocean. *J. Atmos. Sci.* **41**, 3238–3253.

GREENHUT, G. K. & KHALSA, S. J. S. 1982 Updraft and downdraft events in the atmospheric boundary layer over the equatorial Pacific Ocean. *J. Atmos. Sci.* **39**, 1803–1818.

GREENHUT, G. K. & KHALSA, S. J. S. 1987 Convective elements in the marine atmospheric boundary layer. Part I: Conditional sampling statistics. *J. Clim. Appl. Met.* **26**, 813–822.

GRÖTZBACH, G. 1982 Direct numerical simulation of laminar and turbulent Bénard convection. *J. Fluid Mech.* **119**, 27–53.

GRÖTZBACH, G. 1986 Direct numerical and large eddy simulation of turbulent channel flows. In *Encyclopedia of Fluid Mechanics*, vol. 6 (ed. N. P. Cheremisinoff), pp. 1337–1391. Houston: Golf.

GRÖTZBACH, G. & SCHUMANN, U. 1979 Direct numerical simulation of turbulent velocity, pressure and temperature fields in channel flows. In *Turbulent Shear Flows*, vol. I (ed. F. Durst *et al.*), pp. 370–385. Springer.

GUILLEMET, B., JOUVENAUX, S., MASCART, P. & ISAKA, H. 1978 Normalisation des moments du deuxième ordre de la vitesse verticale de l'air et de la température dans la couche limite convective. *J. Rech. Atmos.* **12**, 229–243.

GUILLEMET, B., ISAKA, H. & MASCART, P. 1983 Molecular dissipation of turbulent fluctuations in the convective mixed layer. Part I: Height variations of dissipation rates. *Boundary-Layer Met.* **27**, 141–162.

HESS, G. D., SPILLANE, K. T. & LOURENSZ, R. S. 1988 Atmospheric vortices in shallow convection. *J. Appl. Met.* **27**, 305–317.

HINZE, J. O. 1959 *Turbulence*. McGraw-Hill. 586 pp.

HUNT, J. C. R. 1984 Turbulence structure in convection and shear-free boundary layers. *J. Fluid Mech.* **138**, 161–184.

HUNT, J. C. R., KAIMAL, J. C. & GAYNOR, J. E. 1988 Eddy structure in the convective boundary layer – new measurements and new concepts. *Q. J. R. Met. Soc.* **114**, 827–858.

KAIMAL, J. C., WYNGAARD, J. C., HAUGEN, D. A., COTÉ, O. R., IZUMI, Y., CAUGHEY, S. J. & READINGS, C. J. 1976 Turbulence structure in the convective boundary layer. *J. Atmos. Sci.* **33**, 2152–2169.

KLEMP, J. B. & DURRAN, D. R. 1983 An upper boundary condition permitting internal gravity wave radiation in numerical mesoscale models. *Mon. Wea. Rev.* **111**, 430–444.

KONRAD, T. G. 1970 The dynamics of the convective process in clear air as seen by Radar. *J. Atmos. Sci.* **27**, 1138–1147.

KRISHNAMURTI, R. 1975 On cellular cloud patterns. Part 1: Mathematical model. *J. Atmos. Sci.* **32**, 1353–1363.

LENSCHOW, D. H. & STANKOV, B. B. 1986 Length scales in the convective boundary layer. *J. Atmos. Sci.* **43**, 1198–1209.

LENSCHOW, D. H. & STEPHENS, P. L. 1980 The role of thermals in the convective boundary layer. *Boundary-Layer Met.* **19**, 509–532.

LENSCHOW, D. H., WYNGAARD, J. C. & PENNELL, W. T. 1980 Mean-field and second-moment budgets in a baroclinic, convective boundary layer. *J. Atmos. Sci.* **37**, 1313–1326.

LILLY, D. K. 1967 The representation of small-scale turbulence in numerical simulation experiments. In *Proc. IBM Sci. Comput. Symp. on Environmental Sci., Nov. 14–16, 1966, Thomas J. Watson Res. Center, Yorktown Heights, N.Y., IBM Form* 320–1951, pp. 195–210.

LUDLAM, F. H. & SCORER, R. S. 1953 Convection in the atmosphere. *Q. J. R. Met. Soc.* **79**, 317–341.

LYONS, W. A. & PEASE, S. R. 1972 "Steam Devils" over the Lake Michigan during a January arctic outbreak. *Mon. Wea. Rev.* **100**, 235–237.

MAHRT, L. & PAUMIER, J. 1984 Heat transport in the atmospheric boundary layer. *J. Atmos. Sci.* **41**, 3061–3075.

MASON, P. J. 1987 Large eddy simulation of a convective atmospheric boundary layer. In *Proc. Sixth Symp. Turbulent Shear Flows, September 7–9, 1987, Toulouse, France*, pp. 12-4-1–12-4-4. Extended version to appear in *J. Atmos. Sci.*

MASON, P. J. & CALLEN, N. S. 1986 On the magnitude of the subgrid-scale eddy coefficient in large-eddy simulations of turbulent channel flow. *J. Fluid Mech.* **162**, 439–462.

MASON, P. J. & THOMSON, D. J. 1987 Large-eddy simulations of the neutral-static-stability planetary boundary layer. *Q. J. R. Met. Soc.* **113**, 413–443.

MELLOR, G. L. & YAMADA, T. 1974 A hierarchy of turbulence closure models for planetary boundary layers. *J. Atmos. Sci.* **31**, 1791–1806 (Corrigenda 1977, *J. Atmos. Sci.*, **34**, 1482).

MOENG, C.-H. 1984 A large-eddy-simulation model for the study of planetary boundary layer turbulence. *J. Atmos. Sci.* **41**, 2052–2062.

MOENG, C.-H. & WYNGAARD, J. C. 1986 An analysis of closures for pressure-scalar covariances in the convective boundary layer. *J. Atmos. Sci.* **43**, 2499–2513.

MOENG, C.-H. & WYNGAARD, J. C. 1988 Recent large-eddy-simulation results for the convective boundary layer. In *Eight Symp. on Turbulence and Diffusion, San Diego, April 25–29, 1988*, pp. 41–44. American Meteorological Society, Boston, Mass. Extended version submitted to *J. Atmos. Sci.*

NIEUWSTADT, F. T. M. & DE VALK, J. P. J. M. M. 1987 A large eddy simulation of buoyant and non-buoyant plume dispersion in the atmospheric boundary layer. *Atmos. Environ.* **21**, 2573–2587.

PAULSON, C. A. 1970 The mathematical representation of wind speed and temperature profiles in the unstable atmospheric surface layer. *J. Appl. Met.* **9**, 857–861.

ROWLAND, J. R. & ARNOLD, A. 1975 Vertical velocity structure and geometry of clear air convective elements. In *Proc. 16th Radar Meteorology Conf., Houston, Texas, April 22–24, 1975*, pp. 296–303. Amer. Met. Soc., Boston, Mass.

SCHEMM, C. E. & LIPPS, F. B. 1976 Some results of a simplified three-dimensional numerical model of atmospheric turbulence. *J. Atmos. Sci.* **33**, 1021–1041.

SCHMIDT, H. 1988 Grobstruktur-Simulation konvektiver Grenzschichten. Diss. University of München, report DFVLR-FB-88-30.

SCHUMANN, U. 1975 Subgrid scale model for finite difference simulations of turbulent flows in plane channels and annuli. *J. Comp. Phys.* **18**, 376–404.

SCHUMANN, U. 1987 The countergradient heat flux in turbulent stratified flows. *Nucl. Engrg Des.*, **100**, 255–262.

SCHUMANN, U. 1988 Minimum friction velocity and heat transfer in the rough surface layer of a convective boundary layer. *Boundary-Layer Met.* **44**, 311–326.

SCHUMANN, U., HAUF, T., HÖLLER, H., SCHMIDT, H. & VOLKERT, H. 1987 A mesoscale model for the simulation of turbulence, clouds and flow over mountains: Formulation and validation examples. *Beitr. Phys. Atmos.* **60**, 413–446.

SMOLARKIEWICZ, P. K. 1984 A fully multidimensional positive definite advection transport algorithm with small implicit diffusion. *J. Comput. Phys.* **54**, 325–362.

SOMMERIA, G. 1976 Three-dimensional simulation of turbulent processes in an undisturbed trade wind boundary layer. *J. Atmos. Sci.* **33**, 216–241.

SPALART, P. R 1988 Direct simulation of a turbulent boundary layer up to $R_\theta = 1410$. *J. Fluid Mech.* **187**, 61–98.

STULL, R. D. 1973 Inversion rise model based on penetrative convection. *J. Atmos. Sci.* **30**, 1092–1099.

TURNER, J. S. 1986 Turbulent entrainment: the development of the entrainment assumption, and its application to geophysical flows. *J. Fluid Mech.* **173**, 431–471.

WEBB, E. K. 1977 Convection mechanisms of atmospheric heat transfer from surface to global scales. In *Proc. Second Australasian Conf. on Heat and Mass Transfer, Sydney*, pp. 523–539 (NTIS 77N30685/2).

WEBB, E. K. 1984 Temperature and humidity structure in the lower atmosphere. In *Geodetic Refraction-Effects of Electromagnetic Wave Propagation Through the Atmosphere* (ed. F. K. Brunner), pp. 85–141. Springer.

WILCZAK, J. M. & BUSINGER, J. A. 1983 Thermally indirect motions in the convective atmospheric boundary layer. *J. Atmos. Sci.* **40**, 343–358.

WILCZAK, J. M. & BUSINGER, J. A. 1984 Large-scale eddies in the unstably stratified atmospheric surface layer. Part II: Turbulent pressure fluctuations and the budgets of heat flux, stress and turbulent kinetic energy. *J. Atmos. Sci.* **41**, 3551–3567.

WILCZAK, J. M. & TILLMAN, J. E. 1980 The three-dimensional structure of convection in the atmospheric surface layer. *J. Atmos. Sci.* **37**, 2424–2443.

WILLIS, G. E. & DEARDORFF, J. W. 1974 A laboratory model of the unstable planetary boundary layer. *J. Atmos. Sci.* **31**, 1297–1307.

WILLIS, G. E. & DEARDORFF, J. W. 1979 Laboratory observations of turbulent penetrative-convection planforms. *J. Geophys. Res.* **84**, C1, 295–301.

WOODCOCK, A. H. & WYMAN, J. 1947 Convective motion in air over the sea. *Ann. N.Y. Acad. Sci.* **48**, 749–777.

WYNGAARD, J. C. 1985 Structure of the planetary boundary layer and implications for its modeling. *J. Clim. Appl. Met.* **24**, 1131–1142.

YOUNG, G. S. 1988 Turbulence structure of the convective boundary layer. Part II: Phoenix 78 aircraft observations of thermals and their environment. *J. Atmos. Sci.* **45**, 727–735.

ZEMAN, O. & LUMLEY, J. L. 1976 Modeling buoyancy driven mixed layers. *J. Atmos. Sci.* **33**, 1974–1988.